Near-infrared Imaging for Information Embedding and Extraction with Layered Structures

WEIWEI JIANG, DIFENG YU, CHAOFAN WANG, and ZHANNA SARSENBAYEVA, University of Melbourne, Australia
NIELS VAN BERKEL, Aalborg University, Denmark
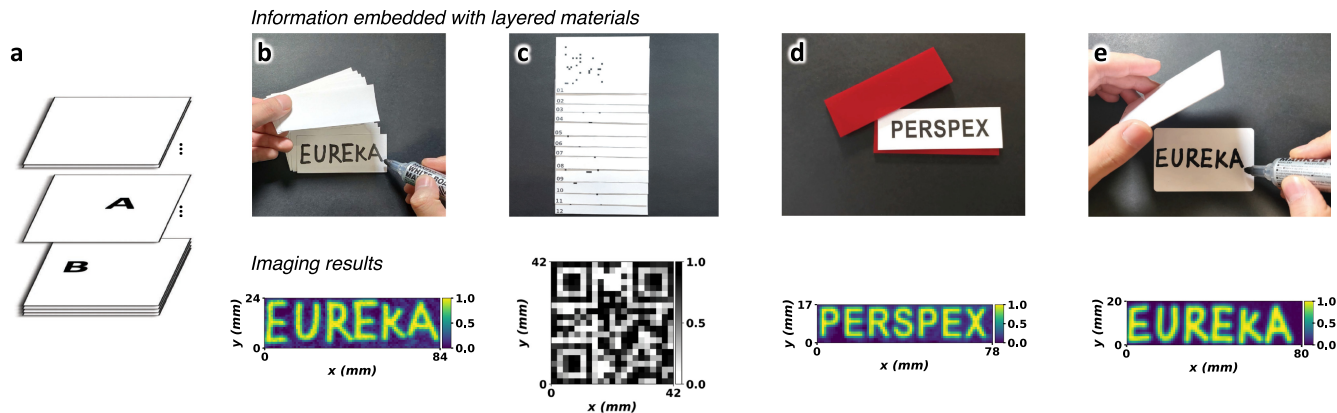JORGE GONCALVES and VASSILIS KOSTAKOS, University of Melbourne, Australia

Fig. 1. We propose a method for practical information embedding and extraction for layered structures as illustrated in (a) and demonstrated by imaging (b) a handwriting content embedded in a 12-page paper stack (for non-destructive reading), (c) a split QR code in a 12-page paper stack (as chipless digital information), (d) a printout inserted between two perspex plates (as a physical tagging layer), and (e) handwriting between two PVC cards (as steganography).

Non-invasive inspection and imaging techniques are used to acquire non-visible information embedded in samples. Typical applications include medical imaging, defect evaluation, and electronics testing. However, existing methods have specific limitations, including safety risks (e.g., X-ray), equipment costs (e.g., optical tomography), personnel training (e.g., ultrasonography), and material constraints (e.g., terahertz spectroscopy). Such constraints make these approaches impractical for everyday scenarios. In this article, we present a method that is low-cost and practical for non-invasive inspection in everyday settings. Our prototype incorporates a miniaturized near-infrared spectroscopy scanner driven by a computer-controlled 2D-plotter. Our work presents a method to optimize content embedding, as well as a wavelength selection algorithm to extract content without human supervision. We show that our method can successfully extract occluded text through a paper stack of up to 16 pages. In addition, we present a deep-learning-based image enhancement model that can further improve the image quality and simultaneously decompose overlapping content. Finally, we demonstrate how our method can be generalized to different inks and other layered materials beyond paper. Our approach enables a wide range of content embedding applications, including chipless information embedding, physical secret sharing, 3D print evaluations, and steganography.

CCS Concepts: • **Computing methodologies** → **Computer graphics**; • **Human-centered computing** → *Ubiquitous and mobile computing*; • **Hardware** → *Emerging optical and photonic technologies;*

Additional Key Words and Phrases: Near-infrared spectroscopy, information embedding, information extraction, non-invasive inspection

1 INTRODUCTION

Information extraction consists of techniques to read contents that are encoded or embedded in a sample, object, or even signal. **Radio-frequency identification (RFID)**, for instance, is one of

the most prevailing technologies for this purpose [Ngai et al. 2008; Sheng et al. 2008]. However, such a technology cannot be adopted to non-digital contents, such as normal printing or handwriting, and it requires a sophisticated embedded chip and functional electronic circuits. Alternatively, in particular, X-ray is widely used as a promising method for not only medical use but also for extracting other embedded contents such as reading an unopened letter as recently demonstrated by Dambrogio et al. [2021].

Despite the prevalence of existing methods on non-invasive content extraction, there are several limitations that constrain their usage in everyday scenarios. Besides X-ray, predominant content extraction methods are mostly used in medical diagnosis, including optical tomography, **terahertz time-domain spectroscopy (THz-TDS)**, ultrasonography, and **magnetic resonance imaging (MRI)** [Chan and Perlas 2011; Hall and Brenner 2008; Huang et al. 1991; Morris 1986; Son et al. 2019]. Despite the maturity of X-ray, it is well known that exposure to X-ray may increase the risk of developing health issues, and thus has restricted usage cases [Hall and Brenner 2008]. A safe alternative such as MRI is also widely used, but it requires certain nuclei with an odd number of protons (mostly H^1 in water for medical imaging) [Morris 1986]. Similarly, ultrasonography is susceptible to extreme changes of sound impedance in samples, which is a common occurrence (e.g., the performance drops sharply when there is a gas between the transducer and the organ of interest in medical ultrasound imaging) [Ortiz et al. 2012]. Alternatively, THz-TDS is challenging to extract content from sub-millimeter layered structure when the signal contrast between the content and the layer material is low in the THz frequency range, which is common in many scenarios with layered structures [Redo-Sanchez et al. 2016].

The limitations of existing methods motivate us to explore a method to embed and read information for more general scenarios, such as for everyday use. In particular, we focus on layered structures as a common use case, as illustrated in Figure 1(a). Example applications include but are not limited to non-destructive reading (such as an unopened letter, mimicked by a paper stack in Figure 1(b)), chipless information embedding (as compared to RFID, demonstrated by a **Quick Response (QR)**-code split into a 12-page paper stack in Figure 1(c)), physical tagging for a layered object (such as a stacked digital fabricated object as shown in Figure 1(d)), and steganography (exemplified by a handwriting content between two PVC cards in Figure 1(e)).

Technically, our method is inspired by optical tomography, a non-invasive imaging technique that can provide both high-resolution images (up to sub-micrometer) and broad spectral information of a sample, and are safe to the human body [Boas et al. 2001; Huang et al. 1991; Ntziachristos 2010]. Although optical tomography has limited penetration ability as compared to other aforementioned techniques, it can still pass through certain materials. A few studies demonstrate that optical tomography can be successfully adopted in other applications such as painting diagnostics [Arecchi et al. 2006] and artefact examinations [Targowski et al. 2004]. However, most existing studies on optical tomography focus on medical use and are considerably customized, making them more costly to generalize to everyday scenarios. This motivates our work using an emerging technology, miniaturized **near-infrared spectroscopy (NIRS)**, which is cheaper,

mobile, and more suitable for content extraction in general scenarios.

Conventionally, NIRS is used for non-destructive analysis in a range of disciplines [Jiang et al. 2021; Klakegg et al. 2016; Siesler et al. 2008]. Its typical applications include food quality control in agriculture [Goel et al. 2015], physiological diagnosis in healthcare [Klakegg et al. 2018; Scheeren et al. 2012], medicine control in pharmaceutics [Roggo et al. 2007], and brain-computer interfaces in computer science [Solovey et al. 2009]. An advantage of the NIRS method is that **near-infrared (NIR)** light can better penetrate samples [Reich 2005], compared to other lights such as visible and ultraviolet lights. Thus, NIRS can be used to acquire information at greater depth. This characteristic enables our adoption of NIRS for occluded content extraction.

In this article, we present a low-cost and generic technique that can embed and extract occluded content in everyday layered structures without any special treatment. The main contributions of our paper are fourfold:

- We demonstrate a prototype and a method to embed contents using normal printouts on commonly used copy paper, such as printed texts, handwriting, and QR codes.
- In addition, we present an unsupervised and non-reference wavelength selection algorithm that can enhance the imaging results, enabling content extraction at greater depths.
- Furthermore, we show a deep-learning-based method to enhance the imaging results, including super-resolution for upscaling, and content-decomposition for separating superimposed contents, at the same time.
- Finally, we demonstrate that our method can be used with various inks, including toner cartridge (laser printer), pigment ink cartridge (inkjet printer), marker pen, rollerball pen, and pencil (2B), as well as a range of layered materials, including perspex (acrylic), **polylactide (PLA)**, vinyl tapes, and **polyvinyl chloride (PVC)**.

2 RELATED WORK

2.1 Non-destructive Testing Methods

Non-destructive testing (NDT) aims to extract an object's internal information, such as its inner structure, material, and composition [Gholizadeh 2016]. With respect to the fundamental principles, commonly used NDT methods include electromagnetic radiation-based techniques, ranging from high-energy X-ray and Gamma-ray imaging, optical tomography, **terahertz (THz)** imaging, to low-energy microwave imaging [Deng and Liu 2011]. While non-electromagnetic methods include ultrasound imaging or ultrasonography [Chan and Perlas 2011], **magnetic resonance imaging (MRI)** [Morris 1986], and so on.

X-ray and Gamma-ray imaging. X-ray and Gamma-ray are ionizing radiations with frequencies between 30 petahertz ($\times 10^{15}$ Hz, PHz) and 300 exahertz ($\times 10^{18}$ Hz, EHz) [Butcher 2010]. They consist of sufficiently high energy to detach electrons from atoms and molecules, and can penetrate many dense materials in a relatively great depth [Martz et al. 2016]. Such properties make X-ray and Gamma-ray ideal for extracting the internal information of an object, while also harmful to living tissue [Hall and Brenner 2008; Zamanian and Hardiman 2005]. Whereas Gamma-ray is

more useful in cosmic studies such as Gamma-ray burst [Meszaros 2006], X-ray can prevail in many scenarios, besides its common applications for airport security [Griffin et al. 2018] and medical diagnosis including projectional radiography [Ducros et al. 2017] and **computed tomography (CT)** [Shepp and Kruskal 1978]. For instance, Stromer et al. utilize a 3D X-ray micro-CT scanner to read a closed book without opening it [Stromer et al. 2017]. However, their approach cannot yield clear images for individual pages. Whereas a recent work by Dambrogio et al. shows more promising results to virtually unfold and read a sealed historical letter with letterlock (a folding technique to seal a letter without an envelope). Specifically, they applied an algorithm to transform a 3D X-ray micro-CT data into a 2D image [Dambrogio et al. 2021]. The authors further demonstrated that the reconstructed images could be successfully transcribed by humans. In addition, Sabetsarvestani et al. present a method to separate X-ray images for artworks painted on both sides, using a self-supervised convolutional neural network [Sabetsarvestani et al. 2019]. Despite the prosperity of X-ray, its adverse impact on the human body is inevitable in principle [Morris 1986], thus cannot be used in everyday scenarios.

Optical tomography. Unlike X-ray or Gamma-ray, optical tomography is safe for the human body [Fercher et al. 2003]. It utilizes infrared or visible lights with frequencies between 300 gigahertz ($\times 10^9$ Hz, GHz) and 790 terahertz ($\times 10^{12}$ Hz, THz), predominated by **near-infrared (NIR)** region with frequencies from 120 to 400 THz (or wavelengths from 2,500 to 750 nm) [Butcher 2010]. Although near-infrared light cannot pass through as many materials as X-ray or Gamma-ray, it can still penetrate certain objects to a specific depth, which outperforms visible lights [Reich 2005]. Common optical tomography techniques include **optical coherence tomography (OCT)**, which is mostly used for medical imaging in ophthalmology or cardiology [Baumal 1999], and **diffuse optical tomography (DOT)**, which is used for brain imaging, breast cancer imaging, monitoring oxygenation changes of **hemoglobin (Hb)** cells in the blood, and other medical applications [Hoshi and Yamada 2016]. Similar to X-ray, optical tomography also has non-medical applications, including non-destructive inspection of artworks, contactless material characterization, data storage, and security [Stifter 2007]. For instance, Arecchi et al. claim the first application of adopting OCT on painting diagnostics [Arecchi et al. 2006]. Specifically, the authors leveraged near-infrared lights centered at 800 nm wavelength with 100 nm bandwidth for measuring the varnish film thickness during a cleaning process for painting conservation. For measuring everyday objects, Czajkowski et al. demonstrate that OCT can be used in quality inspection for a printed RF antenna, focusing on the height of wire profiles, which may impact the antenna's performance [Czajkowski et al. 2010]. Another study on an everyday object was conducted by Alarousu et al. , where the authors use OCT to investigate the properties of papers [Alarousu et al. 2005]. The authors successfully reconstructed a 3D image of a copy paper sample with a 0.16 mm thickness, demonstrating the penetration ability of OCT in an everyday object, with wavelengths centered at 822 nm/832 nm and 20.2 nm/19.7 nm spectral width. In this article, we further study the penetration ability of near-infrared light on everyday objects using NIRS, which is more fundamental than optical tomography.

In addition to tomography, there are other optical imaging technologies using infrared light that may penetrate materials in specific scenarios. For instance, a recent study by Wallace et al. shows a full waveform **light detection and ranging (LiDAR)** system can be used in bad weathers such as heavy rain, fog, or smoke [Wallace et al. 2020]. In particular, the authors leverage near-infrared light with a wavelength at 1,550 nm to penetrate smoke. For far-infrared light, Kowalski et al. show that cloth fiber can be penetrated by long-wavelength infrared using a 7,700 nm/11,500 nm thermal camera, and a 0.25-Terahertz camera [Kowalski et al. 2015], which can be used for revealing concealed items under cloths.

Other non-destructive testing techniques. Besides the aforementioned prevailing techniques, there are other non-destructive testing techniques used in specific fields. For instance, THz imaging, with wavelengths between 1 mm and 10 μm (partially overlapped with far-infrared), has other nondestructive testing applications apart from previous under-cloth item inspection, such as quality inspection of plastics or food [Jansen et al. 2010]. THz imaging is also applied in clinical applications such as endoscopy (examining the inside of a hollow organ) and otoscopy (examining the inside of ears) [Son et al. 2019]. Whereas its main limitation is the high cost of the THz source and detector [Afsah-Hejri et al. 2020], and the detectable blackbody radiation emitted by many materials at room temperature as noise [Hegedüs et al. 2020]. Furthermore, at the end of the electromagnetic radiation spectrum, there are microwave and radio wave imaging techniques with long wavelengths between 100,000 km and 1 mm (or frequency between 3 Hz and 300 GHz). Recent studies have also focused on utilizing Wi-Fi for object or human identification, activity recognition, and imaging, exploiting its ubiquity [Ma et al. 2019]. Whilst its penetration ability is high including solid walls [Adib and Katabi 2013], the Wi-Fi imaging technique is limited to reconstructing the outline of an object's shape at a resolution of meters, or up to tens of centimeters with an emerging 60 GHz Wi-Fi device [Zhu et al. 2017], as a special example of **millimeter-wave (mmW)** imaging [Patel et al. 2016].

Finally, there exist radiography techniques using non-electromagnetic radiations, such as ultrasonography [Chan and Perlas 2011] and **nuclear magnetic resonance imaging (NMRI)**, i.e., MRI [Morris 1986]. Albeit these techniques are exceptionally useful on medical applications for diagnosis, they require highly customized devices for medical use with professional training, and are limited to particular materials (e.g., an object consists of materials with similar acoustic impedance for ultrasonography, or materials with an odd number of protons in nuclei for MRI). Hence, it is challenging to adopt these techniques for radiography in everyday scenarios.

2.2 Information Embedding and Extraction Methods

Broadly speaking, our work also relates to the information embedding and extraction techniques, which aim to encode and decode information inside an object that cannot be detected by human eyes. Besides the aforementioned techniques, recent studies present a variety of methods for such a purpose in everyday settings. Here, we categorize these studies, with respect to the materials used. On the one hand, dielectric materials are rather

transparent to specific electromagnetic or non-electromagnetic radiations while opaque for human eyes, as mentioned previously. Hence, in particular, this property enables information embedding using digital fabrication techniques such as 3D printing and laser cutting, and normal printout on copy papers. On the other hand, conductive materials are opaque to electromagnetic radiations while responsive as an antenna for designated wavelengths, which can also be embedded as information.

Dielectric materials. Existing works using dielectric materials involve at least two materials that have different properties such as scattering or absorbance. For instance, Li et al. present an AirCode scheme to embed information such as a QR code, inside a 3D printed object, using a group of air pockets as the information material with sophisticated designs under the surface [Li et al. 2017]. The air pockets are unnoticeable for human eyes, while readable using an off-the-shelf projector as a patterned light source, and a monochrome linear camera at 700 nm wavelength (i.e., red light). The authors also demonstrated that their method can be generalized to read cut-out texts on paper. However, AirCode cannot work on normal inks, thus, is limited to the scenarios allowing air pockets to be embedded. Similarly, Willis et al. show an information embedding and extraction approach in digitally fabricated layered objects such as 3D print or laser-cut in the THz domain [Willis and Wilson 2013]. The authors also utilize air for information encoding, resulting in similar limitations to AirCode. To generalize the THz imaging technique to normal inks, Redo-Sanchez et al. show a time-gated spectral imaging method that can read texts written by a HB or 6B pencil through nine-layered papers [Redo-Sanchez et al. 2016]. However, their method requires 300 μm thick papers instead of the more common 100 μm thick papers (i.e., 80 gsm papers). Also, the method cannot be applied to laser printer inks or permanent inks due to the low spectral contrast between the ink material and the paper material in the THz domain. Alternatively, Tserevelakis et al. successfully extracts ink-printed information from a four-layer paper stack using the photoacoustic imaging technique with 20 MHz ultrasound [Tserevelakis et al. 2019], while they require samples immersed in distilled water and spaced without direct contact, which is not practical.

Conductive materials. The underlying principles of information embedding and extraction using conductive materials involve designing a conductive pattern that can be detected by specific sensors or performs as a microstrip antenna printed on the circuit board. Above all, one of the most well-known technology for this purpose is **radio frequency identification (RFID)** [Ngai et al. 2008]. However, it is infeasible to integrate RFID circuits in everyday objects, as it requires a well-designed circuit and a dedicated chip for data storage. To address this limitation, researchers are motivated to study the chipless RFID technique that can be printed like a bar code [Herrojo et al. 2019b; Preradovic and Karmakar 2010]. In particular, a state-of-the-art work using a microstrip line encoding scheme achieves a high data density of 26.04 bits/cm^2 [Herrojo et al. 2019a]. Furthermore, a chipless RFID can be inkjet printed [Yang et al. 2007], even with a modified domestic printer [Kawahara et al. 2013]. Nevertheless, chipless RFID techniques are fragile, since they either rely on the electrical resonance properties that require fine capacitance tuning, or other sophisticated but unstable transmission line circuits in general. Also, an
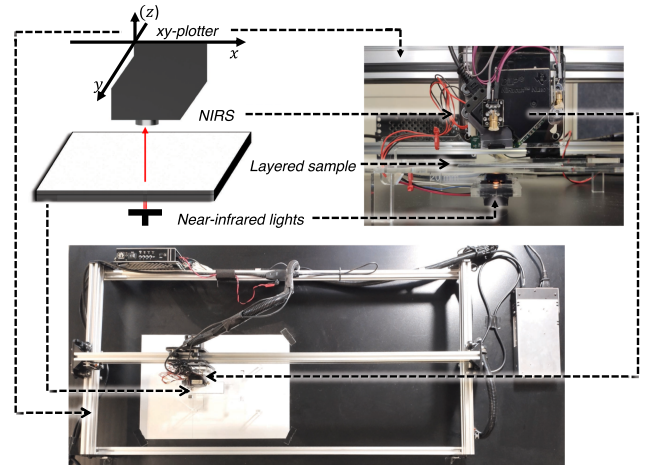

Fig. 2. System setup. A near-infrared spectroscopy (NIRS) scanner is mounted on an xy-plotter for raster scanning. The scanner is configured in transmission mode. A near-infrared (NIR) light source is attached in tandem below the scanner. A layered sample with occluded contents is placed between the light source and the scanner on a transparent acrylic platform.

Fig. 3. Pixel size and scan area. (a) Pixel size is optimum given the scan area. Scans are performed at the center of each pixel. (b) Scans performed at the edge of adjacent pixels can result in indistinguishable signals. (c) Pixel size is too small, each scan includes multiple pixels that cannot be distinguished.

RFID reader can occupy a wide range of already-scarce radio frequency spectrum resources spanning up to several GHz (a chip-RFID is either single-frequency or narrow-band covering tens of MHz) [Herrojo et al. 2019b]. To this end, chipless RFID is still a maturing technique for everyday scenarios.

As a substitute, Chadalavada et al. present an ID'em scheme using an array of conductive dots (i.e., an array of cells with or without conductive dots) for information embedding [Chadalavada et al. 2018]. The conductive dot array can be then detected by an array of inductive sensors decoded as the information, through the covering or finishing materials including wood, felt, glass, acrylic, tile, and concrete. Nonetheless, their method is highly customized with an exceptional information encoding scheme, which is difficult to be generalized to other encoding materials such as normal inks. Compared to the aforementioned works, in this article, we present a method for information embedding and extraction that can be generalized to common objects and inks in everyday settings in the near-infrared region.

3 SYSTEM DESIGN

3.1 Overview

Our system consists of prototype hardware (Figure 2) and software for raster scanning. A miniaturized **near-infrared**
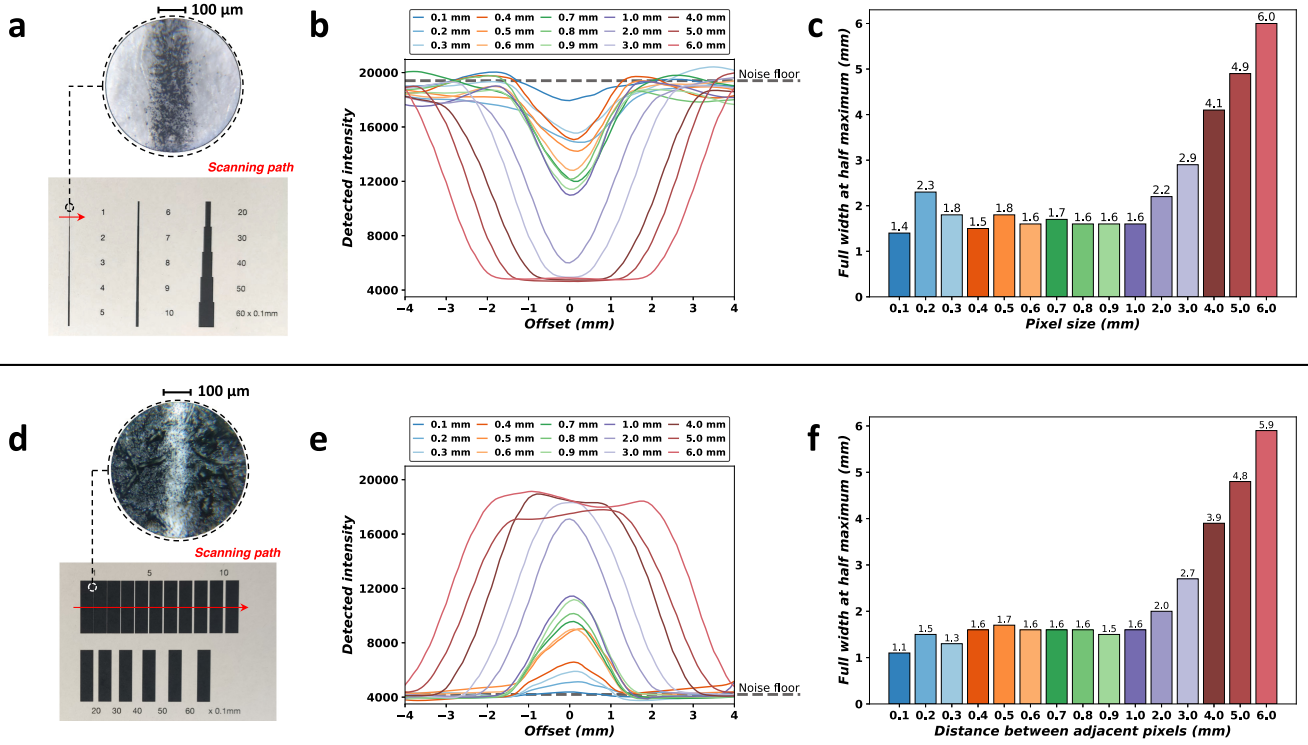
Fig. 4. Pixel size measurement. (a) A printout sample with bars of varying width (between 0.1 mm and 6.0 mm). We scan across each bar from left to right with a 0.1 mm step, as illustrated by the red arrow. (b) For each bar, we calculate the mean intensity levels at different scanning positions, centered around the location with peak absorbance. (c) The half-peak widths in (b) for each bar width. (d) A printout sample with different gap widths. We scan across the bars from left to right with a 0.1 mm step, as illustrated by the red arrow. (e) For each gap, we calculate the mean intensity levels at different scanning positions, centered around the peak transmission point. (f) The half-peak widths in (e) for each gap width.

spectroscopy (NIRS) scanner is mounted on an xy-plotter to raster layered samples. Each sample is placed between the scanner and a **near-infrared (NIR)** light source co-located under the scanner. The sample can consist of multiple sheets of paper, with black-ink printed contents (such as text). The sheets used are the common 80 gsm white copy paper, with each sheet being 100 μm thick. The contents are printed by an unmodified commercial office laser printer with default settings.

For each spatial point on the sample, the scanner measures the light intensities at wavelengths between 900 mm and 1,700 nm, after transmitting through the sample. Since printer ink absorbs more light in specific wavelengths, we can discriminate the spatial points with or without ink by comparing the scanned near-infrared spectra. Furthermore, as the scanner only detects the intensities *after* the light passes through all sample layers, the relative order of different layers has no significant effect on the spectrum. Hence, the extraction of content at different layers has the same performance.

After raster scanning all spatial points on the sample, a normalized heatmap is generated to visualize the detected intensities across all spatial points. In this article, we refer to a scanning result at a corresponding spatial point as a "heatmap pixel." The heatmap is the reconstructed image that represents the occluded content within the layered sample. We note that the intensity levels are unitless numbers representing the output of the scanner

without physical meaning. The intensity levels can be transformed to absorbance with a physical meaning (absorbance $A = \log_{10} \frac{\Phi_e^i}{\Phi_e^t}$, where Φ_e^i is the received intensity levels and Φ_e^t is the transmitted intensity levels). Here, we use the raw intensity levels for the heatmap to prevent numerical issues in practice, as the device may output negative intensities due to noise in the high absorbance region.

3.2 System Specifications

Hardware. The NIRS scanner we use is a DLP NIRscan Nano Evaluation Module by Texas Instruments. The measuring wavelengths range between 900 nm and 1700 nm, with 228 distinct wavelengths (digital resolution). The width for the generated light pattern is 7.03 nm, with 0.635 ms exposure time. Each scan repeats three times internally for noise reduction with only one spectrum returned. The device is configured in transmission mode using a DLP NIRScan Nano Transmissive Evaluation Module by Texas Instruments. We modify the transmission module by separating the lamp and the lens on the receiver side to enable the samples to be placed between the lamp and the device. The device is mounted on an xy-plotter to raster scan the samples.

Software. Our software programmatically synchronizes and controls the raster scanning (move-and-scan). The software is
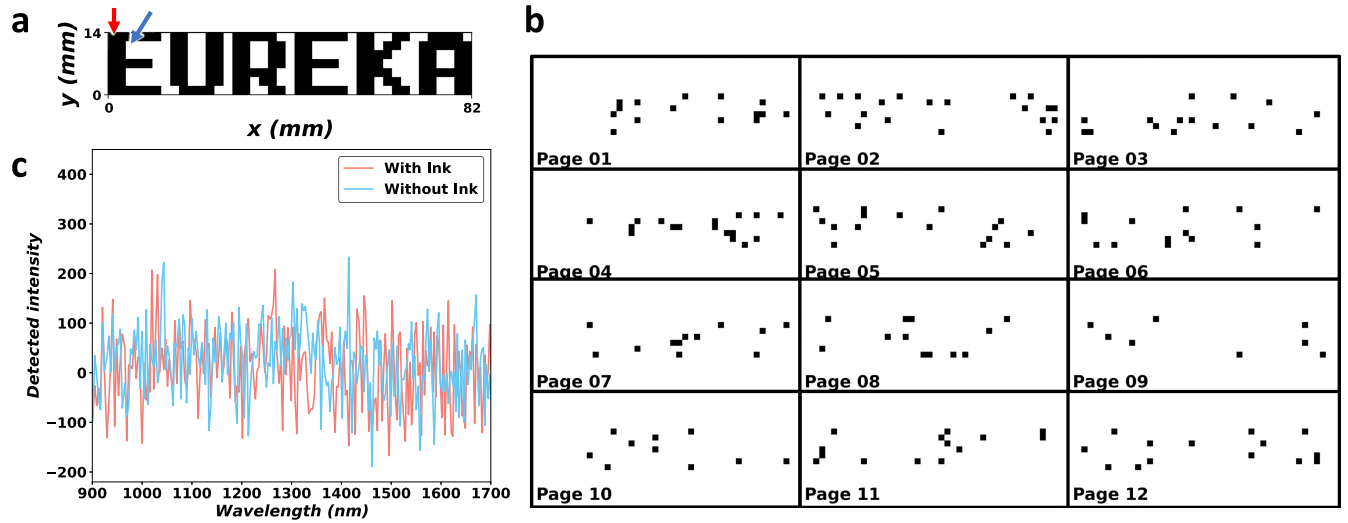
Fig. 5. Sample printout and raw spectra. (a) A pixelated image of "EUREKA" with a 41 × 7 resolution as the ground truth. A red arrow and a blue arrow point to two pixels with and without ink, respectively. (b) The "EUREKA" image is split into 12 pages and printed out. (c) The raw near-infrared spectroscopy spectra for two scans with or without ink respective as illustrated in (b).

developed using Python 3.6 and runs on a normal laptop (HP Pro-Book 440 G6) with a Linux operation system (Ubuntu 18.04.5 LTS). Our algorithm is also developed using Python 3.6. We have open-sourced the software at https://github.com/HighTemplar-wjiang/NIRScanner-Plotter.

3.3 Pixel Size

In practice, the scanner performs a scan through the sample at a small area rather than a point. The size of the area is dictated by the scanner's hardware characteristics. Inevitably, adjacent inked pixels (i.e., areas with printed ink) will interfere with each other if they are close enough when scanned, as illustrated in Figure 3. To overcome this problem, the printed pixel size should, ideally, be *at least* the same size as the scan area. If the printed pixel is smaller, then a single scan is likely to involve multiple printed pixels, which complicates the distinguishing of individual pixels. Further, we note that a scan should be performed at the center of a pixel to minimize signal loss or dispersion. As shown in Figure 3(b), two scans performed at the edge of adjacent pixels will produce indistinguishable results due to the misalignment to the pixels' centers.

In principle, larger pixels are ideal for stronger signal levels but are less practical for imaging. Therefore, as a fundamental parameter, we first need to estimate the minimum viable size for our printed pixels given our scanning setup. For measurement, we scan across printed vertical bars of varying horizontal widths on a single-layered paper. Conceptually, these bars act as one-dimensional pixels. This allows us to measure intensity levels at different positions in relation to the printed area itself, as is shown in Figure 4(a). Specifically, we print bars that range between 0.1 mm and 6.0 mm width. The light's intensity level reaches its minimum level (maximum absorbance) at the center of each bar, and increases when we scan beyond the ink area, as shown in Figure 4(b). In this figure, we consider zero-offsets around the minimum intensity (i.e., maximum absorbance) points. In other words, the pixel's

signal "disperses" around its center. In particular, we calculate the **full width at half maximum (FWHM)** values for each bar as the dispersion area within which an inked pixel can be detected, and pinpoint the zero-offsets as the center of the full width at half maximum region.

As shown in Figure 4(c), for bars thinner than 2.0 mm, the FWHM is consistently and significantly larger than the bar width itself (mean = 1.69, std = 0.23). For bars thicker than or equal to 2.0 mm, the FWHM is approximately equal to the bar width (with error ±0.2 mm). Furthermore, adjacent inked pixels may interfere with each other due to the aforementioned signal dispersion. Accordingly, we also perform measurements of different width gaps (i.e., "negative" pixels) between adjacent bars (Figure 4(d)). We print 5.0 mm bars to maximize the signal level following the results above, as well as to prevent signal dispersion across adjacent gaps. The bars are separated by gaps of varying width between 0.1 mm and 6.0 mm. As shown in Figures 4(e) and 4(f), for the gaps smaller than 2.0 mm, the FWHM is significantly larger than the gap itself (mean = 1.51, std = 0.17). For gaps larger than or equal to 2.0 mm, the FWHM is close to the gap width (with error ±0.3). This result is identical to the aforementioned experiment with different pixel sizes.

Given these results, we chose a pixel size of 2.0 mm as the minimum viable pixel size for our subsequent samples, which represents the optimum trade-off between interference and resolution with our setup.

4 EVALUATION AND WAVELENGTH SELECTION

4.1 Image Quality Evaluation

Using a constant pixel size of 2.0 mm, we evaluate the system performance using pixelated images. As a demonstration, we first pixelate six Latin characters spelling "EUREKA" into a 41×7 pixel resolution image. The pixels are subsequently randomly distributed
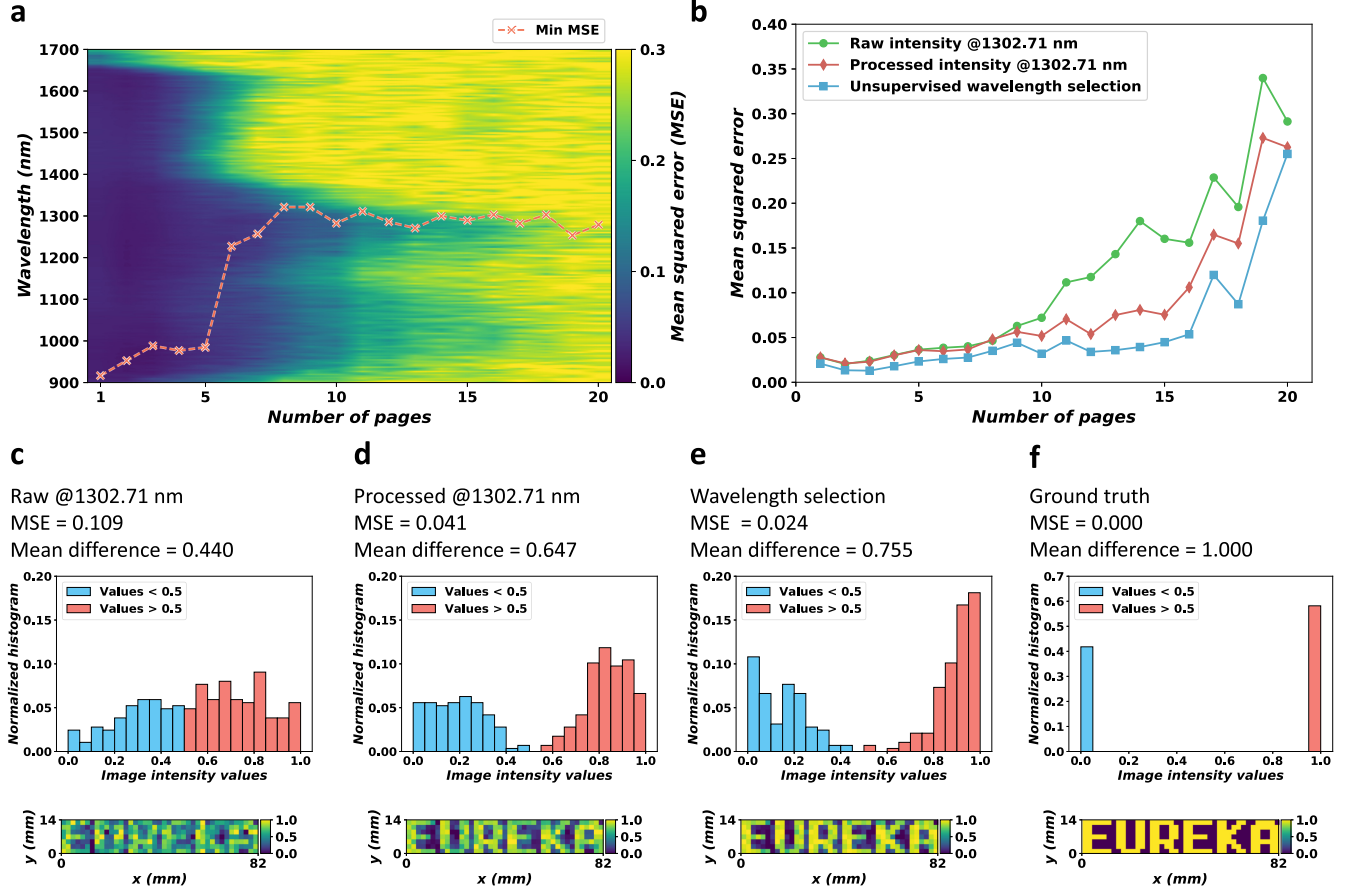
Fig. 6. Mean-squared error (MSE) performance with different number of pages. (a) MSE performance for each wavelength with different number of pages, respectively. A curve shows the minimum MSEs at the corresponding wavelengths. The curve indicates a wavelength around 1300 nm is optimum for the mean-squared error performance. (b) Performance benchmark for different spectrum processing methods. The benchmark is done with a 10×10 randomly generated image. The image is printed and placed on the top of a paper stack for consistency and simplicity. (c–e) Scanning results and their histograms of the EUREKA sample shown in Figure 5, with different processing methods. (f) The ground truth of the EUREKA sample.

across 12 sheets of paper. The sheets are then stacked into a single-layered sample, on which we perform our content extraction. The demonstration image and sample raw spectra are shown in Figure 5. As shown in Figure 5(c), the intensity level is lower for pixels with ink (red arrow, mean intensity = 12.01) than for pixels without ink (blue arrow, mean intensity = 57.68) at certain wavelengths. Also, the raw spectra are noisy as only a small ratio of light can pass through the sample (mean absorbance = 4.72 for a 12-page paper stack, i.e., the mean pass-through ratio is 1.90×10^{-5}).

Next, we systematically measure the effect of varying the number of layers in the sample. Specifically, we vary the number of layers in the sample between 1 and 20. Here, we use a random pattern of 10×10 pixels and containing 50 shuffled inked pixels, as "EUREKA" is a biased sample (does not contain the same number of inked versus non-inked pixels). We include the "EUREKA" sample for demonstration purposes.

To measure the quality of the reconstructed image, we adopt the metric of **mean-squared error (MSE)** between the reconstructed image (i.e., the heatmap) and the ground truth (i.e., the pixelated image) [Wang and Bovik 2009]. A lower MSE value indicates a more accurate reconstruction of the ground truth. We calculate MSE values using reconstructed images at different wavelengths and using a different number of pages. As shown in Figure 6(a), the MSE values are rather small for samples with less than six pages, while the MSE values increase rapidly when more pages are added. Also, for samples with less than six pages, the MSE is smaller at shorter wavelengths (closer to the visible red light), while for thicker samples the MSE is minimized at a wavelength of 1302.71 nm. In general, we observe that specific wavelengths may perform better with smaller MSE values using raw spectra.

This observation motivates our exploration of raw spectra processing and wavelength selection to improve the quality of reconstructed images. Using conventional signal processing tools in literature, we first smooth the raw spectra with a Savitzky–Golay filter (*window size* = 11, *polynomial order* = 3) and a moving average filter (*window size* = 11) [Jiang et al. 2019; Klakegg et al. 2017; Skoog et al. 2013; Zimmermann and Kohler 2013]. Then, the intensity values at the 1,302.71 nm wavelength are selected

for each pixel, respectively, represented by a two-dimensional array. Finally, the intensity values are normalized and drawn to a heat map (values between 0 and 1, where 1 represents an inked pixel). As shown in Figure 6(b), the MSE values with smoothed spectra at 1,302.71 nm are significantly lower than the raw spectra, as also visualized in Figures 6(c) and 6(d) for a clearer EUREKA demonstration.

In addition to single wavelength selection, we further investigate improving the MSE performance using multiple wavelengths, as based on the observation in Figure 6(a). This motivates us to design a wavelength selection algorithm to enhance the reconstructed image. However, it is not realistic to expect to have the ground-truth image available prior to the content extraction procedure. Therefore, the MSE value cannot be used as a variable for wavelength selection. Also, it is not feasible to include a human in the process, i.e., the algorithm must be unsupervised without the ground truth or the reference image. To this end, we developed an unsupervised and non-reference wavelength selection algorithm based on the **mean difference (MD)** between the zero-candidates and one-candidates. A zero-candidate is a pixel with a normalized value less than 0.5 in the heatmap, while a one-candidate is a pixel with a normalized value greater than 0.5. As shown in Figures 6(c) and 6(d), the histogram of the reconstructed image with processed spectra provides a more pronounced split between the two distributions (blue versus red) than when using the raw spectra. This observation is in line with the literature [Bovik 2009]. Next, we quantify the split as the absolute difference between the mean value of the two distributions. Our algorithm aims to search for a wavelength subset that maximizes this mean difference, by adding a wavelength in each iteration. We detail the algorithm and show its performance below.

4.2 Wavelength Selection Algorithm

Our algorithm's performance is shown in Figure 6(b), where it outperforms the conventional signal processing method using the MSE metric. For a visual comparison, we refer to Figure 6(e). In addition, we provide further visual illustration by reconstructing the EUREKA sample for a different number of pages in Figure 7. The reconstructed images appear to be equally clear for an 8-page sample. The image becomes significantly worse for raw spectra with 12 pages, and mostly unreadable with 15 pages. Using the conventional signal processing method, the image is somewhat visible to the human eye up to the 16 page sample. Using our unsupervised and non-reference wavelength selection method, the reconstruction is more accurate, both visually and in terms of MSE score, for all samples up to 16 pages.

The pipeline for our wavelength selection method is illustrated in Figure 8. A Savitzky–Golay filter (*window size* = 11, *polynomial order* = 3) and a moving average filter (*window size* = 11) are adopted to each raw spectrum, respectively, for smoothing before the wavelength selection step. The unsupervised and non-reference wavelength selection algorithm is then applied to select a subset of wavelengths that can reconstruct an optimal image.

The algorithm is described in Algorithm 1. It selects wavelengths recursively by iterating through all wavelengths. The wavelengths are split as a selected wavelength list and an unselected wavelength list, with the selected wavelength list initialized

---

ALGORITHM 1: Non-reference wavelength selection algorithm.

```
input   : A raw spectra array
output  : A reconstructed image, selected wavelengths
/* Initialization. */
1  wavelengthPoll ← all scanning wavelengths;
2  selectedWavelengths, meanDifferences ← ∅;
   /* Begin iterations. */
3  while wavelengthPoll is not empty do
4      maximalMD ← 0;
5      candidateWavelengths ← wavelengthPoll;
6      bestWavelength ← candidateWavelengths[0];
7      foreach wavelength in candidateWavelengths do
8          selectedWavelengths.append (wavelength);
9          currentImage ←
              rawSpectrumArray[selectedWavelengths].norm();
10         currentMD ← calculateMD(currentImage);
11         if currentMD > maximalMD then
12             maximalMD ← currentMD;
13             bestWavelength ← wavelength;
14             bestImage ← currentImage;
15         end
           /* Remove current wavelength for testing next one. */
16         selectedWavelengths.remove(wavelength);
17     end
       /* End of one iteration. */
18     selectedWavelengths.append(bestWavelength);
19     meanDifferences.append(maximalMD);
20     reconstructedImages.append(bestImage);
21     wavelengthPoll.remove(bestWavelength);
22 end
   /* End of iterations. */
   /* Output the iteration with global maximal mean difference. */
23 indexOptimum ← meanDifferences.argMax();
24 return reconstructedImages[indexOptimum],
       selectedWavelengths.firstNItems(indexOptimum +1);
```

---

as an empty set. In each iteration, one wavelength will be selected and moved from the unselected wavelength list to the selected wavelength list, which maximizes the mean difference value. The mean difference values are calculated with the reconstructed image, which is a normalized array after computing the mean intensities for each pixel at selected wavelengths. To alleviate the scaling effect caused by outliers, we also adopted a robust normalization method that uses the 2nd and 98th percentiles as the min-max values. In the end, all wavelengths will be moved to the selected wavelength list ordered by the number of iterations. For our setup, a spectrum consists of 228 wavelengths, thus, 228 iterations will be run for an image. We include extra notes for Algorithm 1 in Appendix Section A.

Through these iterations, after a certain point, the mean difference value of the reconstructed image may decrease after reaching a global maximum. This is because the wavelengths selected later are usually noisy or not responsive to the materials or ink we use. Therefore, as the final step, we need to identify the number of iterations for which the mean difference value is the global maximum. As the selected wavelength list is ordered by the number of iterations, we can simply output the wavelengths indexed from the beginning to the number of iterations.
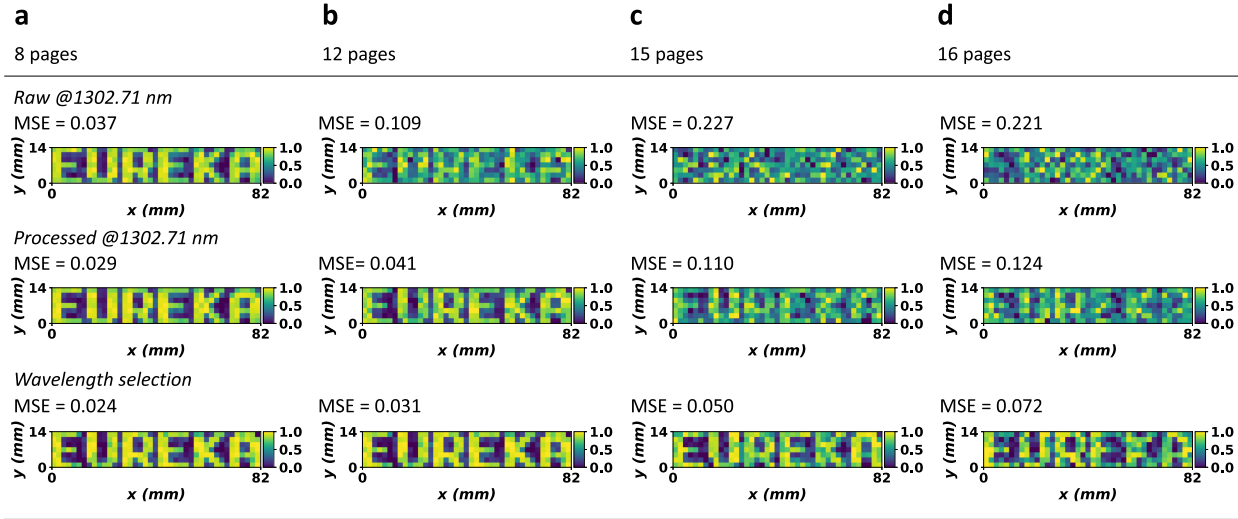
Fig. 7. Scanning results with different number of layers. (a) Scanning results of the EUREKA sample with a 8-page split scheme. All methods show clear imaging outcomes. (b) Scanning results of the EUREKA sample with a 12-page split scheme. Imaging outcome of raw data with single wavelength (@1,302.71 nm) becomes noisy. (c) Scanning results of the EUREKA sample with a 15-page split scheme. Imaging outcome of raw data with single wavelength (@1,302.71 nm) is not readable, while the wavelength selection method still shows a clear imaging outcome. (d) Scanning results of the EUREKA sample with a 16-page split scheme. Imaging outcomes of all methods are noisy, while the wavelength selection method shows a barely readable outcome.
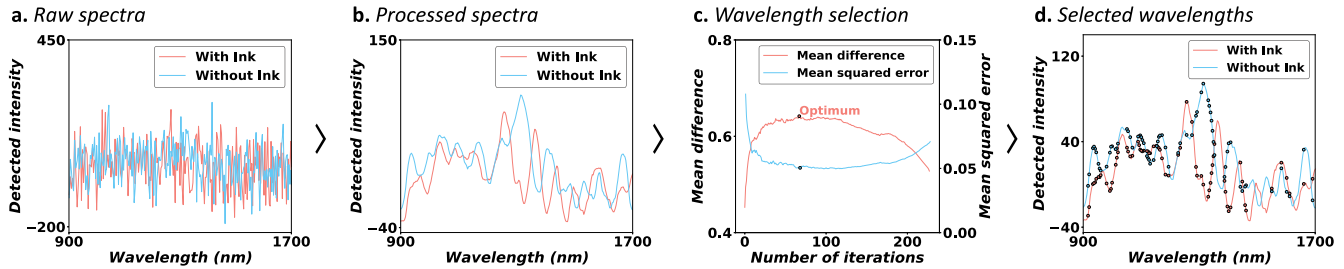

Fig. 8. Signal processing and wavelength selection. (a) Raw spectra for two pixels with or without ink are exemplified, respectively. The layered sample consists of 15 layers of white copy paper. (b) The raw spectra are processed using a Savitzky–Golay filter and a moving average filter. (c) With all the processed spectra, the non-reference wavelength selection algorithm is applied. The optimal point is selected as the wavelength subset with the maximal mean difference. (d) Intensity values at selected wavelengths are averaged as the pixel value (all pixels adopt the same selected wavelength subset).

It is worth noting that, intuitively, our algorithm performs greedy-like steps. At each iteration, the algorithm selects a local optimal wavelength with respect to the mean difference maximization problem, and achieves a decent selection of wavelengths. This is because each selected wavelength carries the most image information and does not cancel out the selected wavelengths that are already in the selection subset in previous iterations. For example, as an extreme case as a result of noise, Wavelength 1 may represent inked pixels as 0 s, while Wavelength 2 represents inked pixels as 1 s. With respect to the mean difference values, both wavelengths are equivalently good, while adding them together would cancel out each other and result in significant information loss. This phenomenon is particularly common in lower intensity cases (e.g., 15 pages). Hence, our algorithm shows a more significant improvement with increasing numbers of pages as illustrated in Figure 7.

Similarly, a straightforward wavelength ranking algorithm may not perform well. For instance, we could consider ranking all the wavelengths by calculating the mean differences, respectively, and then select the top-N wavelengths as the optimal wavelength subset. However, in addition to the above reason, this method falsely assumes that the intensities of different wavelengths are independent. In principle, the NIRS technique is based on molecular overtone and combination vibrations that are very broad in spectrum [Skoog et al. 2013]. Therefore, the measurements among different wavelengths are usually correlated. In addition, depending on the hardware, the noises at different wavelengths may also be correlated. For example, the scanner we use consists of a **digital micromirror device (DMD)** chip for separating the wavelengths that might be a noise source for all wavelengths. In contrast, our algorithm does not require such assumptions and is thus more robust for various system setups and scenarios.

5 IMAGE ENHANCEMENT

Beyond imaging, we now investigate image enhancement methods that can further improve the image quality for practical use. In
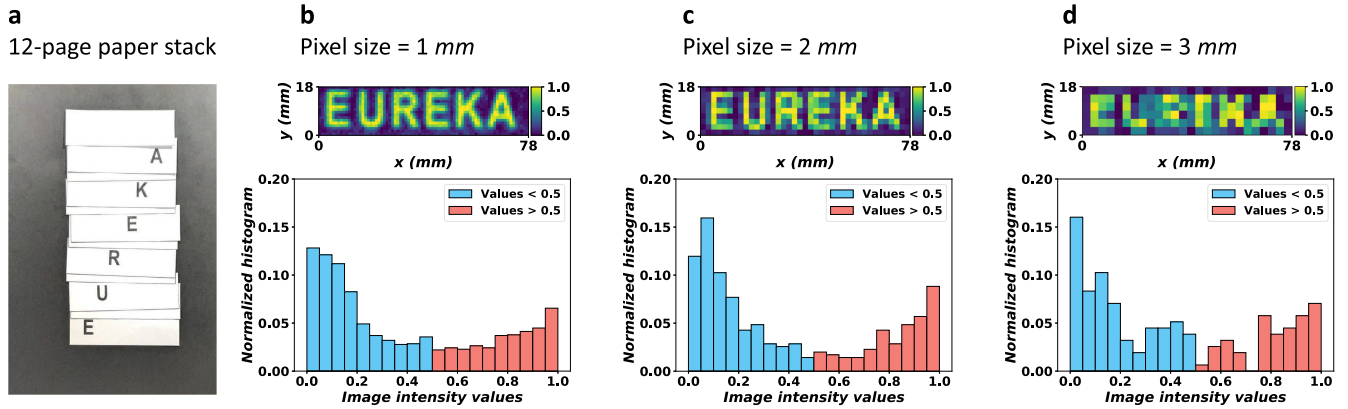
Fig. 9. Sample printout and scanning results with different pixel sizes. (a) Six texts, EUREKA, are printed separately on six pages and stacked with another six empty pages (12 pages in total). (b–d) Scanning results with 1.0 mm, 2.0 mm, and 3.0 mm pixel sizes, respectively.

particular, we present methods that can mitigate the physical limitations of our system, including supersampling, super-resolution, and content decomposition.

5.1 Supersampling

In the reality of the non-digital world, the embedded contents are not pixelated. In such a case, the scanner cannot be expected to optimally align with the sample's pixels. More generally, for instance, handwritten contents consist of ink without a digital context. Hence, we may expect the scan area to be larger than the finer details of the sample, as previously illustrated in Figure 3. Consequently, the reconstructed image can be blurred or jagged (aliasing). Although unavoidable, this issue can be alleviated by using supersampling with a fine resolution [Damera-Venkata and Chang 2009].

For demonstration and comparison, we show the "EUREKA" sample without pixelation in Figure 9(a). The 6 letters of EUREKA are printed on 6 pages, respectively, and interleaved with 6 additional empty papers into a layered sample (thus 12 pages in total). The sample is then scanned using a raster step size of 1.0 mm, 2.0 mm and 3.0 mm, respectively. Varying the raster size means that the plotter driving the NIRS hardware moves in smaller increments across the x and y axes. Consequently, the reconstructed images consist of pixels sized of 1.0 mm, 2.0 mm, and 3.0 mm, respectively. The reconstructed images are shown in Figures 9(b)–9(d). All three images are well-constructed as indicated by the histograms (mean differences are 0.632, 0.675, and 0.637 with 1.0 mm, 2.0 mm, and 3.0 mm pixel sizes, respectively). However, the 3.0 mm pixel-sized image is blurred and some letters are barely distinguishable. The 2.0 mm pixel-sized image is clear and all letters can be easily identified, as well as jagged with aliasing. Finally, the supersampled image with 1.0 mm pixel size is both clear and smooth as expected. These findings suggest that our prototype can extract analog content from layered samples, with anti-aliasing by supersampling.

5.2 Super-resolution and Content Decomposition

Improving Image quality. Beyond supersampling for image enhancement, we further consider two limitations that are con-

strained by physical principles. First, while supersampling is effective for improving the image resolution, the method is limited by the pixel size (2 mm) as shown in Section 4. Increasing the resolution using supersampling results in blurred edges, as shown in Figure 9. A conventional method using the deconvolution process requires certain assumptions to be fulfilled that can be unrealistic (e.g., perfect or accurately estimated **point spread function (PSF)** [Rossmann 1969]). Alternatively, the latest deep-learning-based method is less constrained on such assumptions and more effective on such tasks [Wang et al. 2018]. Hence, in particular, here we show that a **generative adversarial network (GAN)**-based deep-learning approach can further improve the image quality including deblurring, denoising, as well as further improving the image resolution beyond super-sampling (i.e., super-resolution).

Content decomposition. A second physical limitation is the overlap of contents. In principle, our system images the embedded contents as a projection by penetrating the layered structure. Consequently, contents located at the same projection position across different layers overlap in the imaging outcomes. To separate the overlapping contents, we perform a content decomposition process to reconstruct images with non-overlapping content. Effectively, the content decomposition (also known as image decomposition) task can also be well accomplished by using the deep-learning-based approach as the state-of-the-art. To this end, as an end-to-end combined solution, we develop and train a GAN-based deep-learning model to perform both tasks simultaneously.

Deep-learning-based approach. In particular, we adopt a deep adversarial decomposition framework [Zou et al. 2020] incorporating a U-Net convolutional network model [Ronneberger et al. 2015]. Although previous work shows that such a model can be successfully applied to image decomposition tasks [Zou et al. 2020], existing methods only show results on specific public datasets (e.g., dogs and flowers [Khosla et al. 2011; Nilsback and Zisserman 2006]) and cannot be applied directly to our scenario. Therefore, we train a model from scratch for decomposing overlapping contents (e.g., texts) extracted by near-infrared imaging. We include the details for the model and training process in Appendix B.
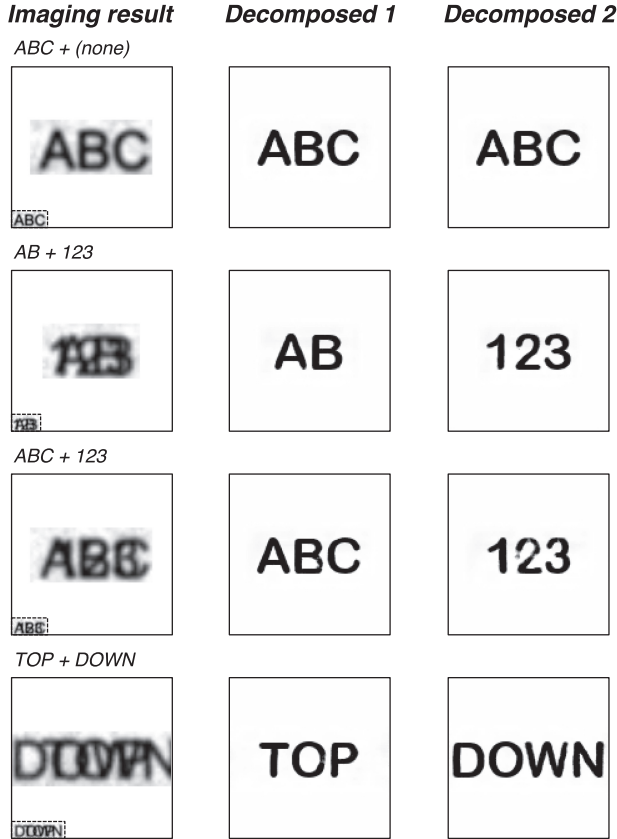
Fig. 10. Results of our deep-learning-based content decomposition with super-resolution model. Left: Near-infrared imaging results (2.5× upscaled with bilinear interpolation, and padded to the 128 × 128 resolution). Left-bottom corner represents the original resolution (inputs). Middle and right: Decomposed images (outputs).

Our results are illustrated in Figure 10, representing different conditions, including non-overlapping, partially overlapping, and fully overlapping cases. The inputs are the near-infrared imaging results with eight-layered white-copy paper stacks (embedded with printout contents "ABC" + none, "AB" + "123," "ABC" + "123," and "TOP" + "DOWN," respectively). The inputs are scaled-up (2.5×, bilinear) and padded to a 128 × 128 resolution. The outputs are two decomposed images (both with a 128 × 128 resolution) for each input image. We can observe that our model can successfully separate overlapping contents. As a special case, the non-overlapped condition is considered as two identical overlapped contents. Beyond content decomposition, our model also performs denoising and deconvolution-like processes (deblurring), yielding clear images with super-resolution.

It is worth noting that our deep-learning-based approach does not conflict with our wavelength selection algorithm (Algorithm 1). Whereas the wavelength algorithm aims to extract as much information as possible from the raw signals (image formation), the deep-learning model performs post-processing to further interpret and improve the image outcomes (image processing).
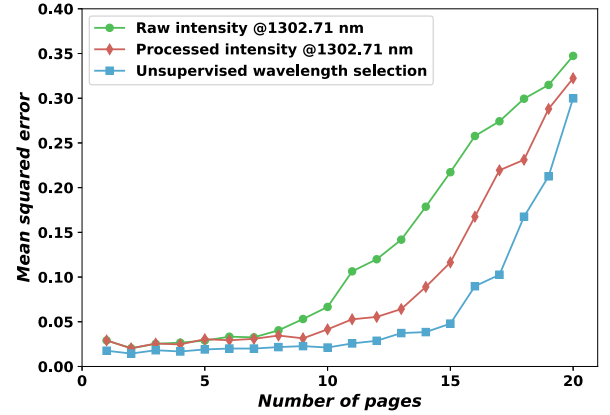

Fig. 11. Mean-squared error (MSE) performance using an inkjet printer with different number of pages.

6 VALIDATIONS AND GENERALIZATIONS

6.1 Other Inks

We next validate and generalize our method with other inks. In total, we test six different inks, including toner cartridge (laser printer), pigment ink cartridge (inkjet printer), marker pen, rollerball pen, ballpoint pen, and pencil (2B).

Inkjet printer. For the two printers, we evaluate the MSE performance using a randomly generated 10 × 10 binary matrix as mentioned in Section 4, since the printers can yield accurate and homogeneous printouts specified by the ground truth (i.e., the binary matrix). The MSE performance for inkjet printer (pigment ink cartridge) is shown in Figure 11. Compared to the laser printer (toner cartridge), the inkjet printer shows similar results as shown in Figure 6.

Pens. In contrast, the MSE evaluation for pens can be unrealistic. It is required to hand-draw the content precisely and homogeneously (i.e., the same amount of ink for all pixels) as per the ground truth (i.e., the binary matrix). Such a scenario is not practical for actual use cases. To this end, we validate the performance using pens in a semi-systematic and realistic form. We hand-write the letters "EUREKA" on white copy paper using different pens. The letters are sketched and filled with pens. We subsequently image the content (EUREKA) with different numbers of pages (8, 12, 15, and 16). The results are shown in Figure 12. Overall, the content written by three pens (marker pen, rollerball pen, and 2B pencil) can be successfully imaged with similar results. In the extreme cases (15 and 16 pages), the marker pen shows slightly better results than the other two pens (rollerball pen and pencil). We are unable to detect significant signals for the ballpoint pen.

6.2 Other Layered Materials

Furthermore, we generalize our method to different materials besides copy paper. We test different materials that are commonly used in everyday scenarios and can be layered. In particular, we test generic copy papers (80 gsm, which is the most common category for printing), perspex (also known as acrylic, a common material for laser cutting), polylactide (PLA, a common material
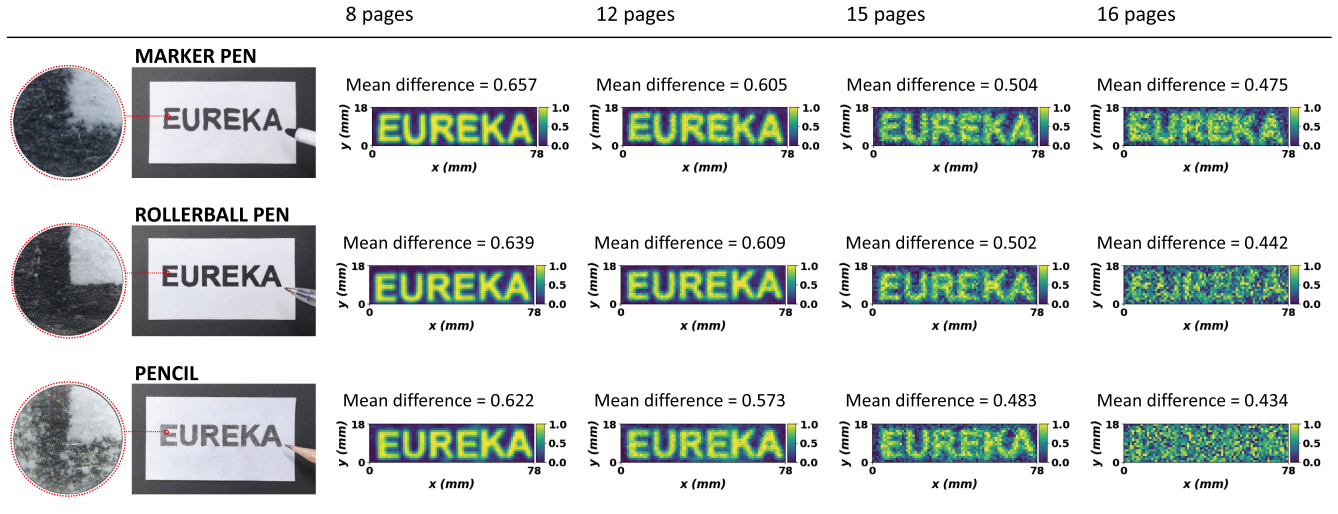
Fig. 12. Imaging results of handwritten contents using different pens (inks), including marker pen (top), rollerball pen (middle), and 2B pencil (bottom).

for 3D printing), and Vinyl tapes (also known as electrical tape, a flexible and opaque tape) with three colors (white, red, and black). We also test medium-density fibreboard (MDF, a commonly used wooden material for hardware prototyping, furniture, and building), polyvinyl chloride (PVC, one of the most popular plastic materials), and copper sheet (a metal material mostly used for electronics).

To establish a limit of how deep we can embed content, we first measure the maximum penetrable layers (thickness) of these materials without ink. In particular, we calculate the absorbance per mm for each material as a measure of penetrability. The process for each material is as follows:

(1) *Data collection*: We scan each sample 100 times in a 10 mm × 10 mm area with 1.0 mm raster steps. We scan an area instead of a fixed position to minimize measurement bias and avoid outlier-related issues. Each material is scanned with varying numbers of layers (thickness) until no signal could be detected by the scanner.

(2) *Spectrum processing*: We then process the absorbance spectra using the same method as reported in Section 4 (smoothed by a Savitzky–Golay filter and a moving average filter).

(3) *Characteristic wavelength selection*: Next, we select the characteristic wavelength for each material by choosing the wavelength with the best linearity. Here, we do not use the MSE-based selection method as in Section 4 to focus on the material itself. Also, it is infeasible to print contents on all materials like paper. As a measurement of the linearity, for each wavelength, we run F-tests using the thickness of the sample as the independent variable, and the absorbance value at each wavelength as the dependent variable. We select the wavelength with the maximal F-value as the characteristic wavelength for that material.

(4) *Linear regression*: Finally, we adopt a linear regression model with the **ordinary least squares (OLS)** method for the characteristic wavelength, respectively, for each material. The estimated coefficient of the linear regression model is regarded
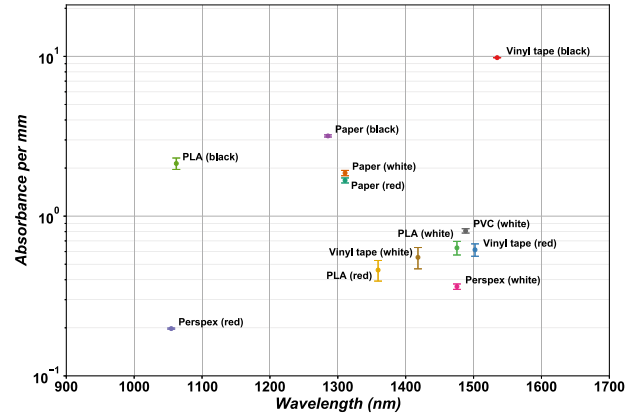

Fig. 13. Absorbance per **mm** values for tested layered materials. The error bars represent the root mean-squared errors (RMSE).

as the value of absorbance per mm for the corresponding material. In addition, due to the limitation of the NIRS scanner, we only consider absorbance values between 2.0 and 5.0 for linear regression, since the thickness-absorbance relationship is non-linear for the absorbance region below 2.0 [Liu et al. 2018]. It should be noted that this phenomenon does not affect our content extraction procedure. Also, the spectra are quite noisy for absorbance beyond 5.0 (i.e., only 10^{-5} ratio of light is detected). Therefore, we consider 5.0 as the maximal absorbance that can be measured by our scanner.

The results for different materials are shown in Figure 13 and listed in Appendix Table E.1. We also provide photos of the samples with microscopic images of their microstructures, as well as the linear regression fitting curves in Appendix E (Appendix Figures E.6–E.10). In summary, both the white and the red copy papers show similar absorbance profiles in the near-infrared region (between 900 nm and 1,700 nm) with maximum 15 and 16 pages penetrable, respectively. While absorbance of the black copy
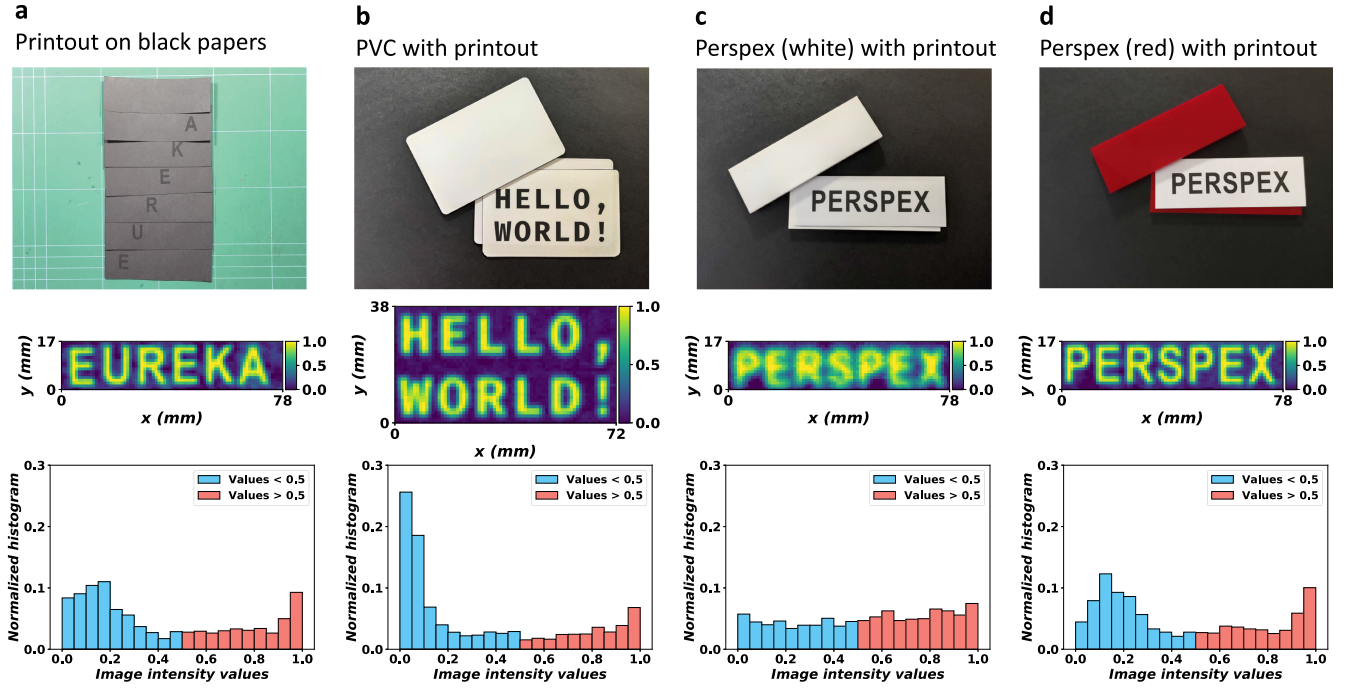
Fig. 14. Samples with different materials. (a) A printout sample with a seven-page black copy paper stack (0.56 mm thickness) and its scanning result (mean difference = 0.616). (b) A printout sample stacked between 2 PVC cards (1.62 mm thickness) and its scanning result (mean difference = 0.686). (c) A printout sample stacked between two white perspex plates (6.00 mm thickness) and its scanning result (mean difference = 0.525). (d) A printout sample stacked between two red perspex plates (5.86 mm thickness) and its scanning result (mean difference = 0.606).

paper is higher, it is still penetrable up to 11 pages. Compared to the copy papers, the perspex materials are more translucent with a substantially lower absorbance for both the white and the red colors. However, we cannot detect any signal for the black perspex with a single layer (2.92 mm). The 3D printing materials, **polylactide (PLA)**, also show a high transmittance (i.e., low absorbance) in the near-infrared region, topped by the red color while bottomed by the black color. Similar results are obtained for the vinyl tapes. Among all the penetrable materials we measured, the black vinyl tape has the most absorbance per mm. Finally, we observe low absorbance for the polyvinyl chloride (PVC plastic) material, while no signal can be detected for the 2.94 mm medium-density fibreboard (wooden material) and the 0.1 mm copper sheet (metal material), hence they are opaque in the near-infrared region with such thicknesses.

6.3 Other use Cases

Next, we demonstrate the feasibility of content extraction with different materials, as a means to show the generalizability of our prototype and our method, as illustrated in Figure 14. First, we print "EUREKA" on 6 pages of black copy paper and cover it with another blank page. Since the absorbance of the black copy paper is higher than the white copy paper, the sample only consists of 7 pages (0.56 mm) instead of 12 pages (1.20 mm). The image reconstructed by our algorithm is very clear, despite the low contrast between the ink and the paper (mean difference in image intensity values = 0.616). In addition, we also test layered samples stacked with

printed white copy paper and PVC or perspex. The reconstructed images are distinct for both the PVC-paper sample (mean difference = 0.686) and the red perspex-paper sample (mean difference = 0.606), while rather blurred for the white perspex-paper sample (mean difference = 0.525) due to higher absorbance. It should be noted that these three mixed samples are much thicker than the paper samples as the materials have a lower absorbance per mm.

In addition, we show content extraction using our system with handwriting using a marker pen. As shown in Figure 15, six letters, "EUREKA" are handwritten on white copy paper and a PVC card, using a normal black marker pen. The handwritten paper is then placed in the middle (Page 7 from bottom to top) of a 12-page stack, while the handwritten PVC card is placed on the bottom and covered by another blank PVC card. Measurements for both samples yield sharp reconstructed images using our prototype and our unsupervised and non-reference wavelength selection algorithm.

6.4 Validation and Comparison with a SWIR Camera

Finally, we validate and compare our method with a SWIR camera (WiDy SenS 640 G-STE). In contrast to our system, which consists of a high spectral resolution and a low spatial resolution, a normal SWIR camera does not separate individual wavelengths while having a higher spatial resolution. Hence, a SWIR camera can be an alternative to our system for imaging purposes. To validate, we demonstrate the imaging results in Figure 16, using a white copy paper stack embedded with the "EUREKA" content. Albeit the SWIR camera can successfully extract the embedded

a
Handwriting on paper
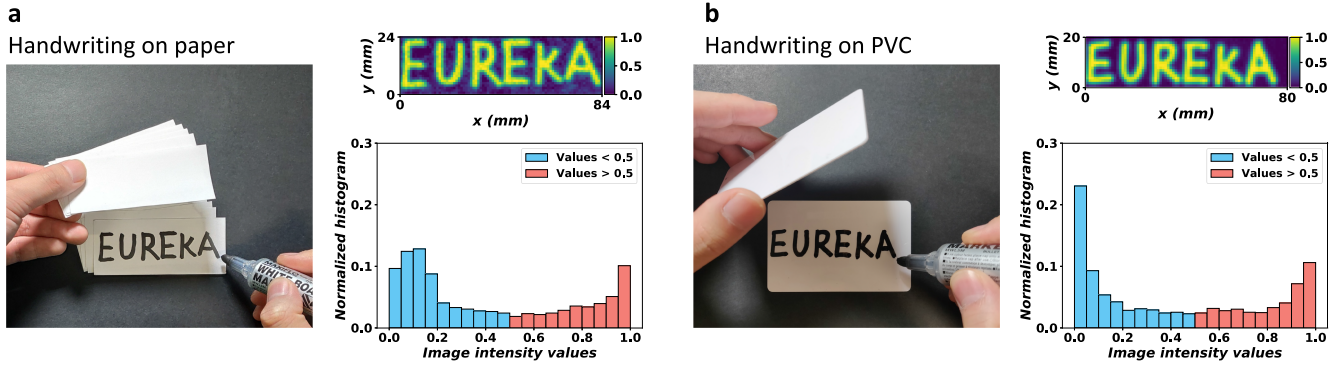

b
Handwriting on PVC

Fig. 15. Handwriting samples with different materials. (a) A handwriting sample on paper within a 12-page paper stack (1.20 mm in total) and its scanning result (mean difference = 0.654). (b) A handwriting sample on PVC within a two-layer PVC stack (1.52 mm in total) and its scanning result (mean difference = 0.678).

information, the noise level is higher due to the high density of thermal agitation of the InGaAs sensor array. From 12 pages onward, the content is overwhelmed by the noise. One possible solution to mitigate this issue is to use a deep-cooling system, although this solution is costly and unpractical for common use cases due to the cooling peripherals (e.g., tubing with coolants). Alternatively, the use of a more powerful light source may increase the penetrated light intensity. However, common light sources such as halogen lamps also emit significant far-infrared lights (heat) that can increase the thermal noise levels.

Furthermore, we note that SWIR cameras are not suitable for evaluation purposes. First, wavelength analysis is more challenging using SWIR cameras as it requires a dedicated tunable bandpass optical filter to select individual wavelengths at a time (i.e., hyperspectral imaging). Also, absorbance evaluation requires uniform illuminance distribution on the sample surface (e.g., paper stack). It further requires three conditions to be met: (1) Ideal parallel alignment for "camera–sample–NIR light source." (2) Ideal parallel NIR light source. (3) A well-controlled space without unwanted stray NIR lights reflected from the NIR light source.[1] Although we adopt a brightness homogenization process to mitigate the illuminance distribution issue (see Appendix C), the absorbance analysis remains challenging as the actual incident lights are not well controlled.

In contrast, our setup intrinsically fulfills the aforementioned requirements with a common laboratory setup. In addition, commercial SWIR cameras are quite expensive, and are therefore not be affordable for common use. For example, the uncooled mid-end SWIR camera we used above is priced at ∼20,000 USD, which is around 20 times more expensive than our system (∼1,000 USD).

7 DISCUSSION

7.1 Applications

Our method shows promising results in content extraction across a range of layered materials, including printouts and handwriting on normal copy paper, as well as other layered materials frequently
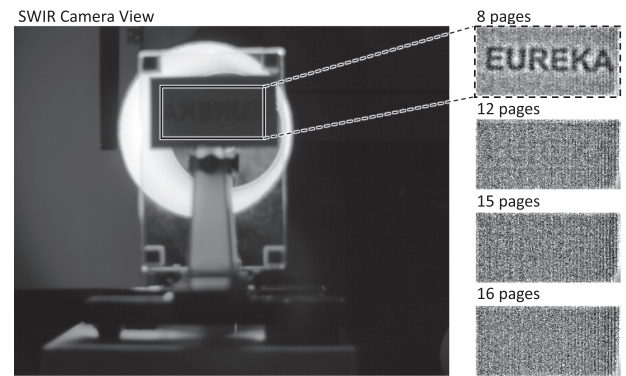

Fig. 16. Imaging results using a SWIR camera. The sample area is cropped out and re-normalized with brightness homogenizing. The camera setup and full results are shown in Appendix C.

used for prototyping. Our method enables a variety of applications leveraging occluded content extraction, such as physical secret sharing [Beimel 2011], steganography using materials that are invisible but responsive in the near-infrared region (such as a synthesized polymer presented by Yamane et al. [2018]), defect inspection in layered structures [Kim et al. 2011], or encapsulated objects such as drugs, covered paintings, or other objects that can be penetrated by near-infrared light [Arecchi et al. 2006]. To demonstrate a practical use case, we develop a physical secret-sharing scheme with QR codes in Appendix Section D. Also, as our method is unsupervised and does not require a reference image, it can be adopted in various use cases with minimal to no effort on sample preparation, calibration, and training.

7.2 Limitations

A major factor that limits the use of this technique is material absorbance in the near-infrared region. Although typically near-infrared light can penetrate further into the samples as compared to ultraviolet, visible, or even mid-infrared lights [Reich 2005], it still cannot pass through certain materials, in particular conductive materials. For instance, our device did not detect any signal with the 0.10 mm copper sheet. In fact, conductive materials are

---

[1]In our test, we found that environmental NIR light was negligible. Stray NIR lights are from the scattering and reflections of the light source.

difficult to penetrate for most electromagnetic waves in principle, and are therefore commonly used for shielding [Geetha et al. 2009].

Another limitation is in relation to overlapping we show in Section 5.2. Although we demonstrate that such a limitation can be mitigated by using a deep-learning-based content decomposition algorithm, training such models for different content types can be non-trivial. Alternatively, the NIRS device can be configured in reflection mode with different light paths that can distinguish reflections at various depths [Arimoto et al. 2005]. However, using the reflection mode will reduce the penetrable depth, since the light must pass through a doubled path, and will have additional intensity loss at the bottom layer due to transmission, absorption, or both if the bottom layer is not 100% reflective at all wavelengths.

Furthermore, our prototype takes advantage of low-cost hardware and components, which lowers the bar for development and deployment. Yet, this limits the capability of our system with lower transmitted light intensity and higher noise levels. Although this issue has been alleviated by our unsupervised and non-reference wavelength selection algorithm, it remains impossible to extract content when no signal is detected. In addition, although our prototype is not bulky, it is not mobile either. This issue can be easily resolved by using a lightweight plotter, whereas we used a generic plotter intended for heavy-duty work such as a **computer numerical control (CNC)** router or a laser cutter.

8 CONCLUSION

In this article, we present a near-infrared imaging method that can be used for information embedding and extraction. Using a miniaturized NIRS scanner, an xy-plotter, and a novel wavelength selection algorithm, we demonstrate that our prototype can successfully read occluded texts through up to 16 pages of papers in everyday scenarios. We also demonstrate different image enhancement methods that can further improve the imaging results in practical use cases. Finally, we show that our method can be generalized

to several inks, including toner cartridge (laser printer), pigment ink cartridge (inkjet printer), marker pen, rollerball pen, and pencil (2B), as well as other layered materials, including perspex (acrylic), polylactide (PLA), vinyl tapes, and polyvinyl chloride (PVC) of different colors. Our work provides a computational perspective on the possibility of practical content extraction using a spectroscopic method in the near-infrared region, enabling a wider range of applications beyond content extraction such as chipless information embedding, physical secret sharing, 3D print evaluations, and steganography.

APPENDICES

A NOTES FOR ALGORITHM 1

Additional details on Algorithm 1.

rawSpectrumArray: A three-dimensional array with index order $(x, y, wavelength)$. Each element represents the light intensity of $wavelength$ at coordinate (x, y).

wavelengthPoll: A one-dimensional array including indexes of unselected wavelengths. The array is initialized as $[0, 1, \ldots,$ N-1] where N is the number of total wavelengths ($N = 228$ for our system).

norm() function: The $norm()$ function includes two steps: (1) calculating the intensity means at selected wavelengths; (2) performing robust normalization of the image array values between 0 and 1. The raw intensities at each wavelength should not get normalized first as it may also amplify the noise. In particular, a wavelength with a greater intensity scale usually represents higher penetration capability to the material (potentially less noisy). Therefore, normalizing intensities before taking the mean will also equalize the noise level that is not desired.

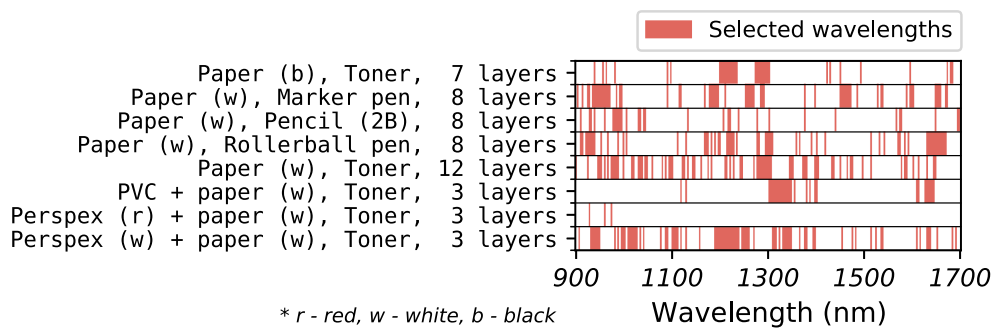Examples of wavelength selection results are illustrated below:

Fig. A.1. Wavelength selection results for different samples.

B SUPER-RESOLUTION AND CONTENT DECOMPOSITION MODEL

The model and training details of our GAN-based deep-learning model for super-resolution and content decomposition, as reported in Section 5.2.

B.1 Model Parameters

Architecture. The model is adopted from the literature [Zou et al. 2020], including three components:

(1) A Generator that separates overlapped contents and generates decomposed images (contents). The generator is a 14-layered U-Net that has been shown effective for various image processing tasks [Ronneberger et al. 2015]. Both input and output sizes are 128×128. For our NIR images that are low-resolution, the images are first up-scaled using the nearest resampling filter (keep ratio), and padded to 128×128.

(2) A Separation Critic that measures if the generated images are well separated or still mixed (overlapped). The Separation Critic is a four-layered Fully Convolutional Network (FCN) [Long et al. 2015] with an input size of 64×64.

(3) Two Markovian Discriminators that measure if the generated images are like real images (i.e., texts-like images). Both Discriminators are three-layered FCNs with input size of 128×128.

Loss function. We use the crossroad per-pixel loss with L1 error (i.e., Mean Absolute Error or MAE) [Willmott and Matsuura 2005]. **Optimizer.** We adopt the AdamW optimizer [Loshchilov and Hutter 2017], with $\beta_1 = 0.5, \beta_2 = 0.999$.

B.2 Training Process

To the best of our knowledge, no existing pre-trained model or dataset exists for our task. Therefore, we created our own dataset for training. As the deep-learning model requires a significant amount of training data with accurate labeling, it is infeasible nor necessary to collect the data manually. Instead, we introduce a process, as described next, to generate the training and test data algorithmically. As we have shown in Section 5.2, the trained model using generated data can be successfully applied to actual near-infrared imaging outcomes.

Training data. We first randomly generate 5,000 images with different texts. Each image includes 1–4 alphabet-numbers that are randomly selected from the alphabet-numeric set. Then, for each training data point, we randomly choose and compose two of these images as overlapping contents. The composition process consists of two steps: (1) Adding two images (pixel values are normalized to $[0, 1]$). (2) Clipping values greater than 1 ($imageArray[imageArray > 1] = 1$). Furthermore, for data augmentation, each composed image is scaled down to a lower resolution. The resolution is randomly determined between 32×32 and 128×128. Next, a Gaussian blur filter is performed with kernel size = 1, with a probability of 0.5 (i.e., half of the images are not Gaussian blurred). Finally, the composed image is again scaled up to 128×128 to serve as input to the model.

Test data. We generated 1,000 images using the same process as the training data for testing. However, we note that the generated data are only for training and validation purposes. The results we show in Section 5.2 are actual NIR imaging outcomes by scanning overlapping samples.

Labels. For each training data, the label contains the two original images for composition. It is worth noting that the original images are clear and high-resolution. Hence, the model is trained to generate clear and high-resolution images, even with blurred and low-resolution images. To this end, the model is trained to generate super-resolution and clear contents besides decomposition.

Training parameters. In total, 2,000 epochs were trained using one Nvidia GeForce RTX 3090 graphics card for 13 h. We set the learning rate = $1e − 4$, with 0.1 decay rate every 1,000 epochs, and batch size = 16. We show samples of training inputs and outputs in Appendix Figure B.2.

Inputs	Q9H	KUWL	FSL0	6Q6	Q4BCC	1CRBH
Outputs 1	L4	P07Z	GD1	676	4B0	CR4
Outputs 2	Q91	KUWL	FSL0	JQL	QNCC	1QBH

Fig. B.2. Samples of training inputs and outputs (predictions) at the end of training (Epoch 2,000).

C SWIR CAMERA TEST

In this section, we include imaging results using a SWIR camera. The camera setup is shown in Appendix Figure C.3, the results are illustrated in Appendix Figure C.4.

Brightness homogenization. We adopt the following steps for homogenizing brightness:

(1) Duplicate the image, then apply a Gaussian blur filter (kernel size = 5).
(2) Invert the blurred image.
(3) Overlay the inverted image and the original image (alpha = 0.5 for both images).
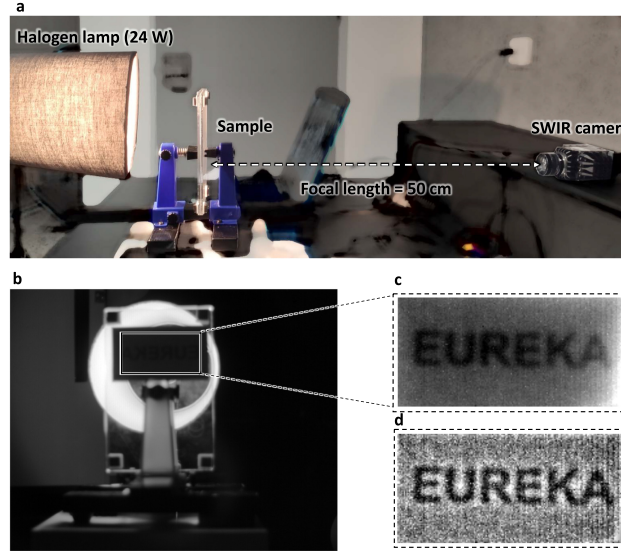

Fig. C.3. Experimental setup using a SWIR camera. (a) Experimental setup with a halogen lamp (left) as the NIR light source, a stacked stamp (middle) and a SWIR camera (right). (b) SWIR camera snapshot example (8 pages). (c) Region of Interest (ROI) with respect to the sample. The ROI image is re-normalized using the robust normalization method (2nd and 98th percentiles). (d) Example image after homogenizing brightness.
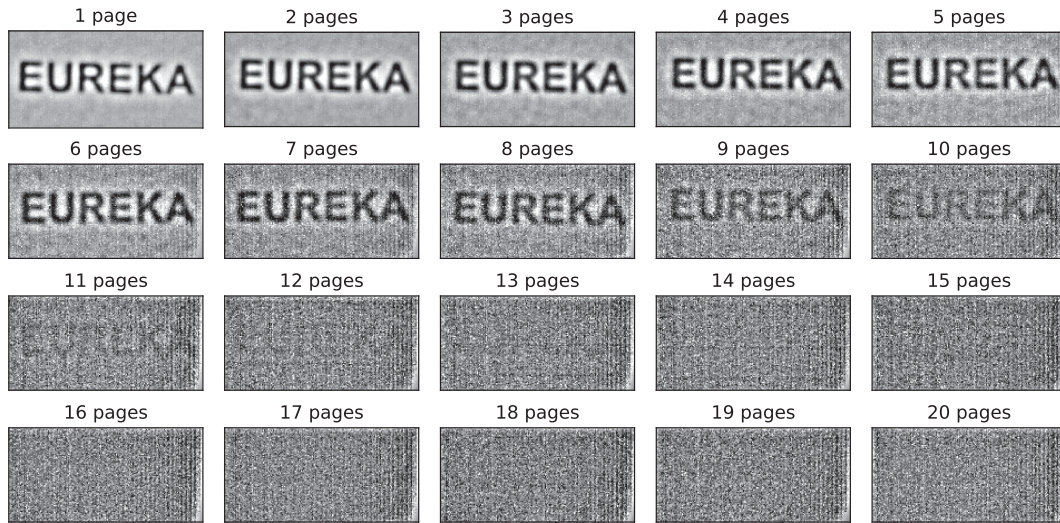

Fig. C.4. SWIR camera imaging results.

D SPLIT QR-CODE EXAMPLE

As shown in Appendix Figure D.5, a 21 × 21 QR code (Version 1, with up to 152 data bits depending on the error correction level) is split into 12 pages that can be distributed as 12 pieces of a secret. To reveal the secret, all 12 pages should be stacked, in any arbitrary order, and scanned using our prototype. It is worth noting that a QR code is actually encoded with an error-correcting code (such as Reed-Solomon or low-density parity-check code). By adjusting the parameters of the error-correcting code (possibly resulting in non-standard QR encoding), one may further control the possible number of absences, such that revealing the secret with only 10 of the 12 pieces is adequate, or defining a critical piece that is required to reveal the secret. Furthermore, this use case can be extended into three-dimensional scenarios, where different information can be revealed from different perspectives (such as 3D printing).
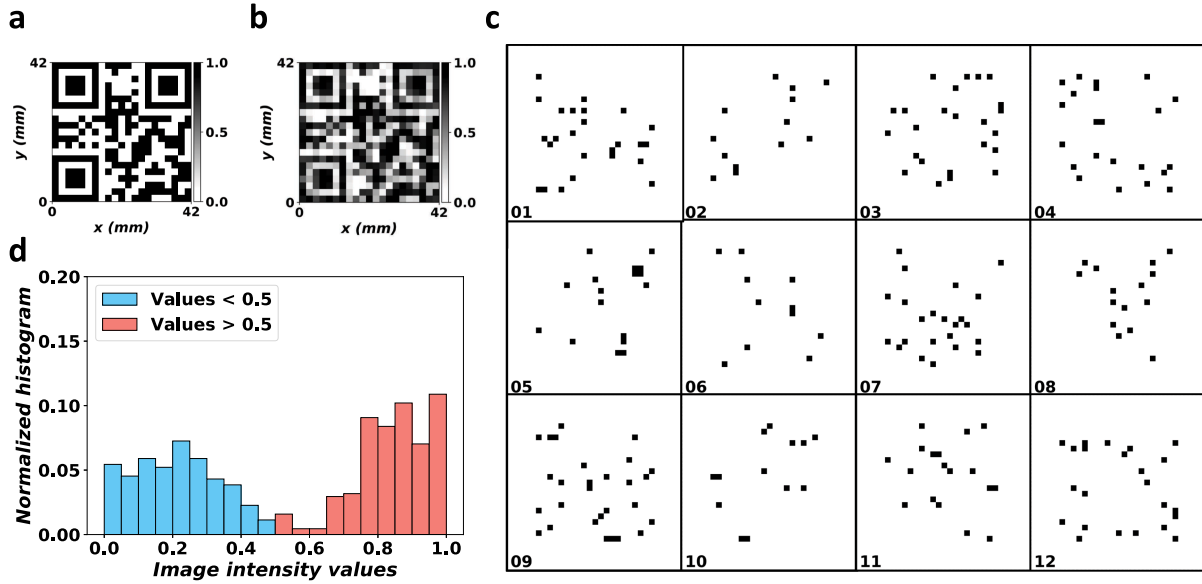

Fig. D.5. A QR-code sample with secret-sharing. (a) The ground truth of the QR code (decodes as "EUREKA"). (b) The reconstructed image of the 12-page paper stack (the image is scannable with a smartphone QR code app). (c) A 12-page split scheme for the ground-truth QR code. (d) The histogram of the scanning result.

E LAYERED MATERIALS

Here, we include the details of tested layered materials.

Table E.1. Tested Materials with Layered Structures

Layer Material	Thickness per layer*	Penetrable layers	Absorbance per mm
Copy paper 80 gsm (white)	0.10 mm	15 (1.50 mm)	1.86 ± 0.07 @1310.71 nm
Copy paper 80 gsm (red)	0.10 mm	16 (1.60 mm)	1.67 ± 0.06 @1310.71 nm
Copy paper 80 gsm (black)	0.08 mm	11 (0.88 mm)	3.18 ± 0.05 @1285.50 nm
Perspex (white)	2.95 mm	2 (5.90 mm)	0.36 ± 0.01 @1475.48 nm
Perspex (red)**	2.88 mm	3 (8.64 mm)	0.20 ± 0.00 @1054.62 nm
Perspex (black)	2.92 mm		*(No signal detected)*
Polylactide (white)	1.00 mm	6 (6.00 mm)	0.55 ± 0.08 @1418.06 nm
Polylactide (red)**	1.00 mm	8 (8.00 mm)	0.46 ± 0.07 @1359.33 nm
Polylactide (black)	1.00 mm	2 (2.00 mm)	2.14 ± 0.18 @1062.06 nm
Vinyl tape (white)	0.18 mm	26 (4.68 mm)	0.63 ± 0.06 @1475.48 nm
Vinyl tape (red)	0.18 mm	26 (4.86 mm)	0.62 ± 0.05 @1502.11 nm
Vinyl tape (black)	0.18 mm	2 (0.36 mm)	9.82 ± 0.01 @1534.72 nm
Medium-density fibreboard	2.94 mm		*(No signal detected)*
Polyvinyl chloride (white)	0.76 mm	4 (3.04 mm)	0.81 ± 0.03 @1488.30 nm
Copper sheet	0.10 mm		*(No signal detected)*

*We measured the actual thickness, respectively, instead of using the claimed thickness of the material products for practice.

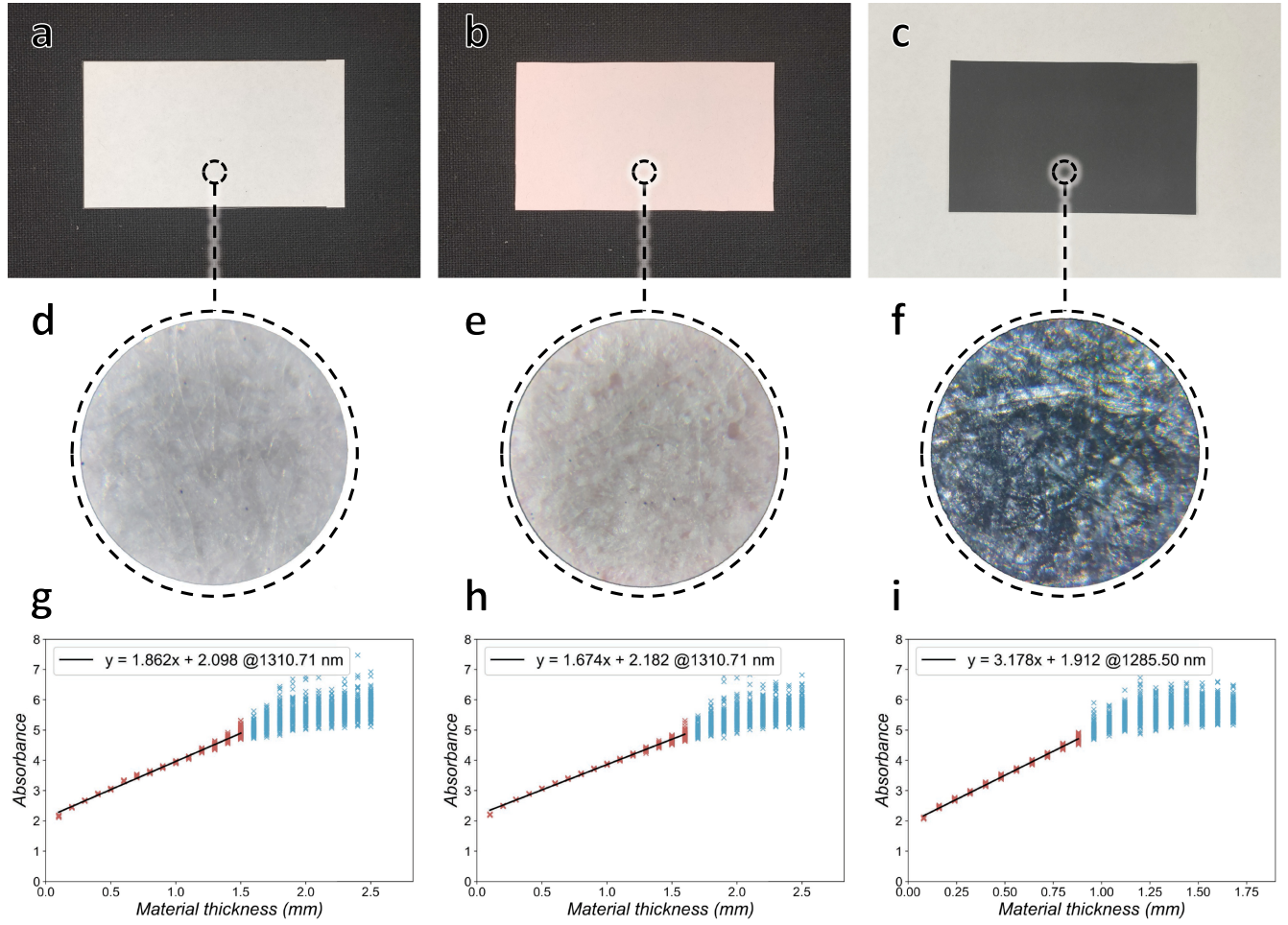**Due to the height limitation in the scanning area, we cannot scan materials thicker than 9.0 mm.

Fig. E.6. Copy paper samples in white (left), red (middle), and black (right). (a–c) The photos of the samples. (d–f) The microscopic views of the samples (500X). (g–i) The linear regression fitting curves at the characteristic wavelength. Data points in linear region (with absorbance between 2.0 and 5.0) are in red, while the data points in non-linear region are in blue.
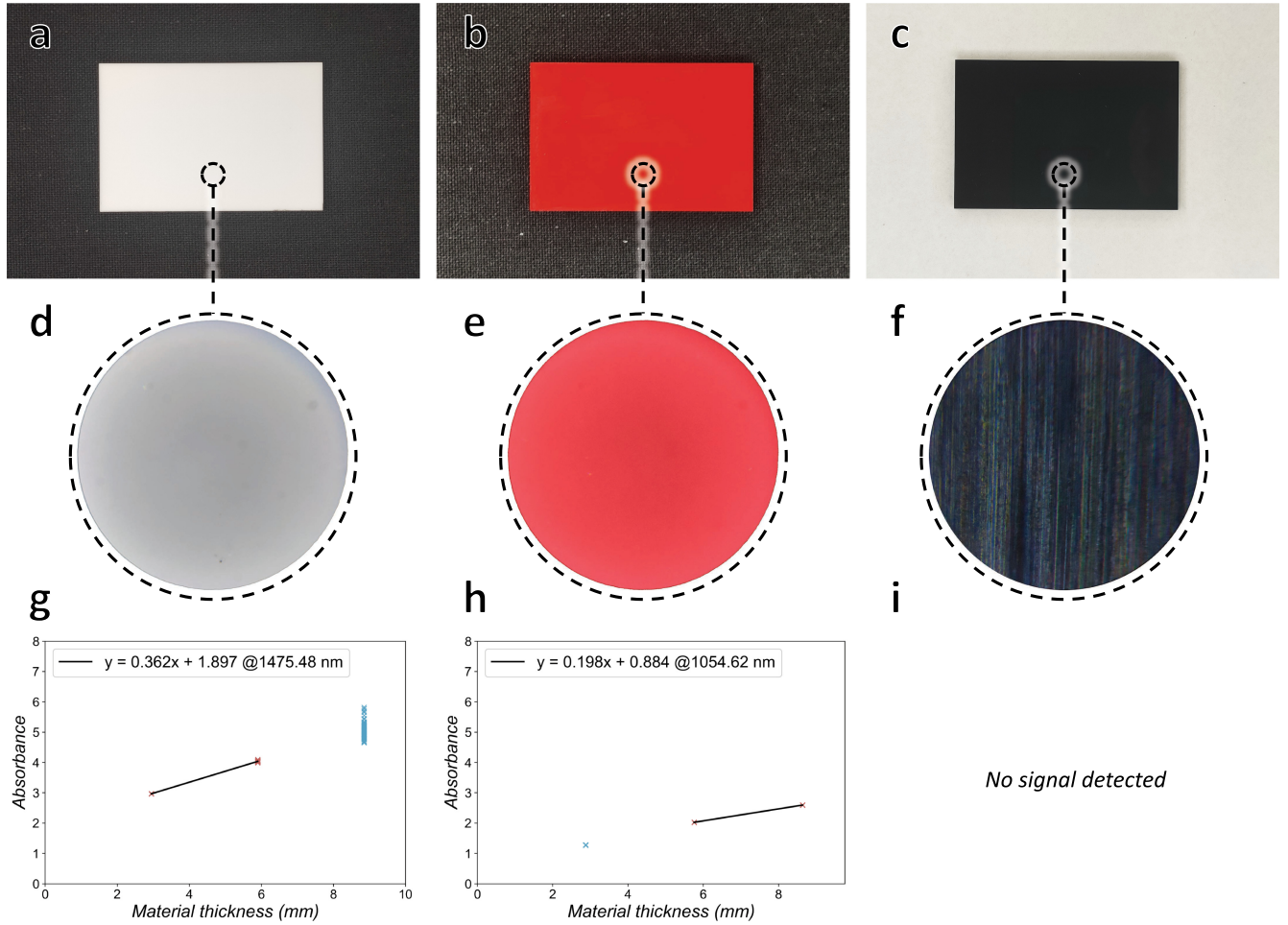
Fig. E.7. Perspex samples in white (left), red (middle), and black (right). (a–c) The photos of the samples. (d–f) The microscopic views of the samples (500X). (g–i) The linear regression fitting curves at the characteristic wavelength. Data points in linear region (with absorbance between 2.0 and 5.0) are in red, while the data points in non-linear region are in blue.

Fig. E.8. Polylactide (PLA) samples in white (left), red (middle), and black (right). (a–c) The photos of the samples. (d–f) The microscopic views of the samples (500X). (g–i) The linear regression fitting curves at the characteristic wavelength. Data points in linear region (with absorbance between 2.0 and 5.0) are in red, while the data points in non-linear region are in blue.
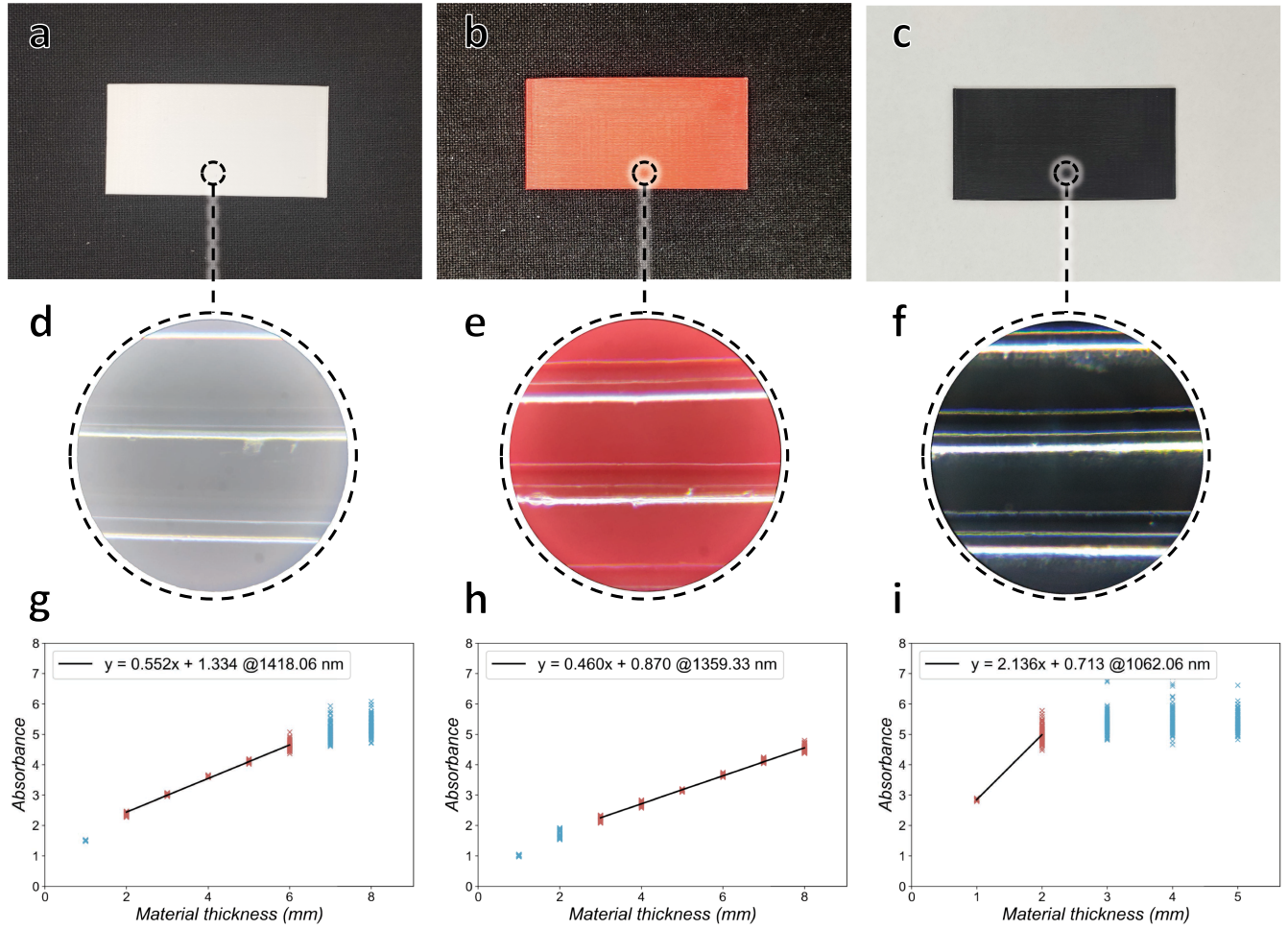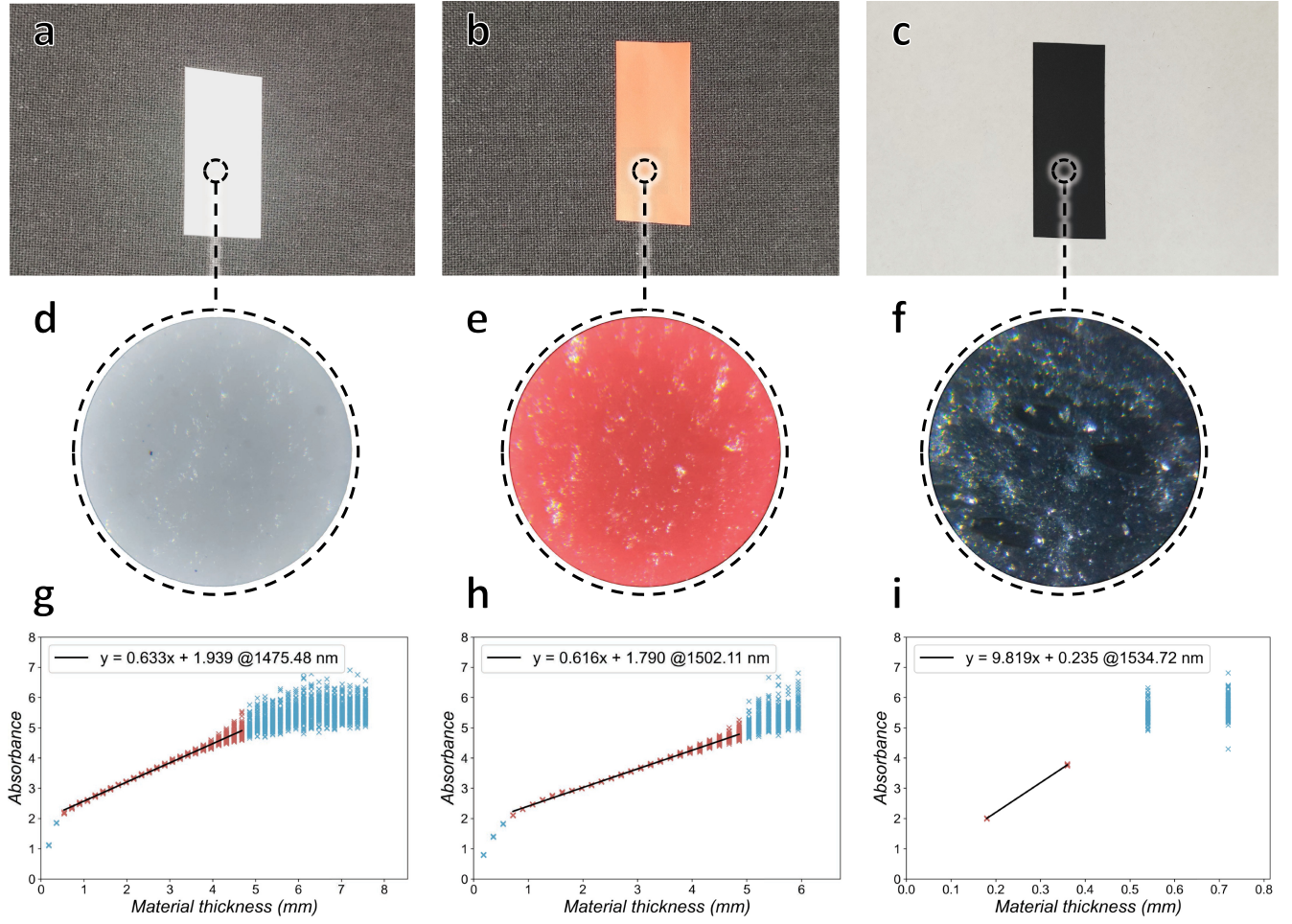
Fig. E.9. Vinyl tape samples in white (left), red (middle), and black (right). (a–c) The photos of the samples. (d–f) The microscopic views of the samples (500X). (g–i) The linear regression fitting curves at the characteristic wavelength. Data points in linear region (with absorbance between 2.0 and 5.0) are in red, while the data points in non-linear region are in blue.
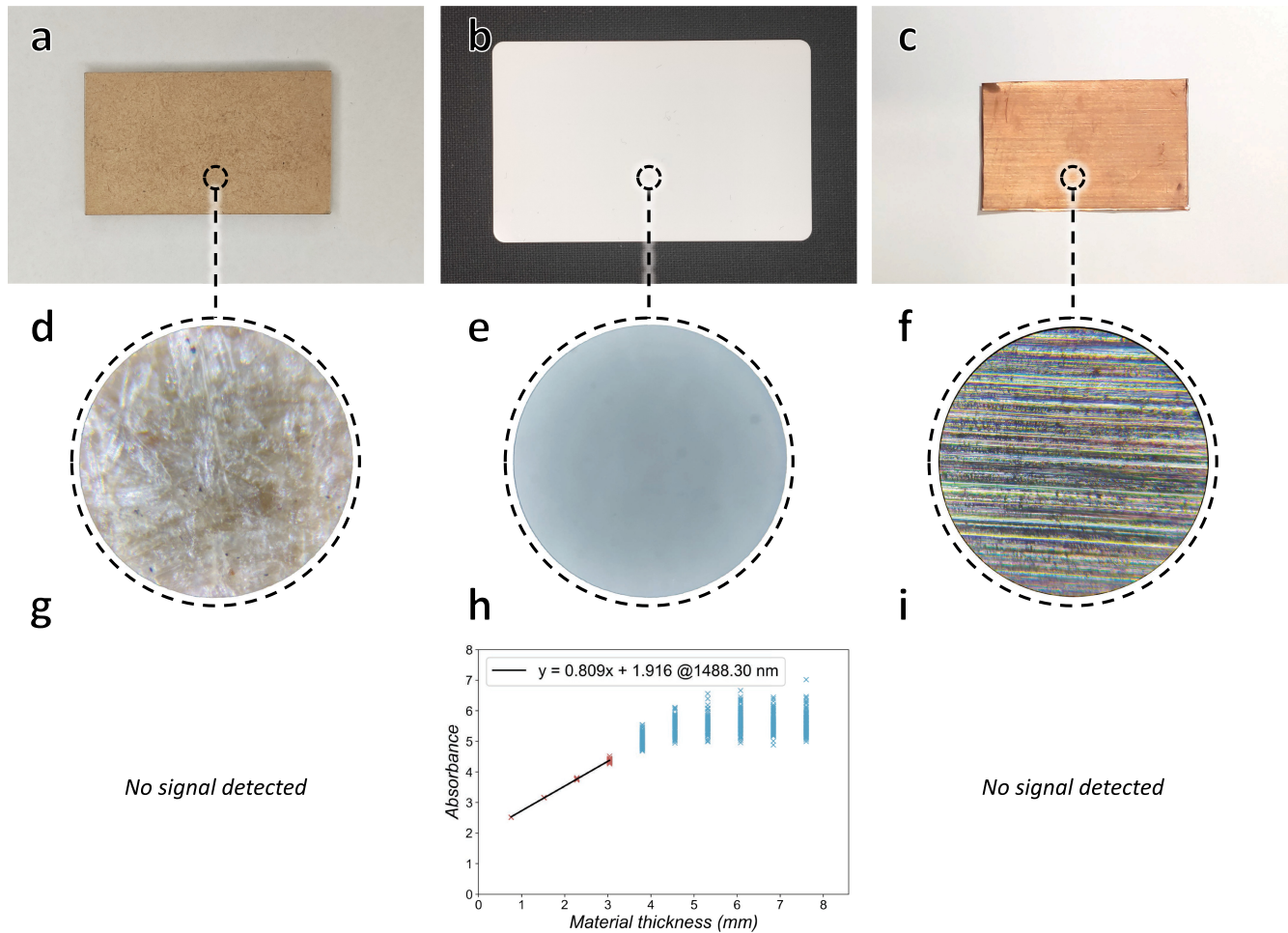
Fig. E.10. Samples of medium-density fibreboard (MDF), white polyvinyl chloride (PVC), and copper sheet. (a–c) The photos of the samples. (d–f) The microscopic views of the samples (500X). (g–i) The linear regression fitting curves at the characteristic wavelength. Data points in linear region (with absorbance between 2.0 and 5.0) are in red, while the data points in non-linear region are in blue.

REFERENCES

Fadel Adib and Dina Katabi. 2013. See through walls with WiFi! In *Proceedings of the ACM Conference of the Special Interest Group on Data Communications (SIGCOMM'13)*. 75–86. https://doi.org/10.1145/2486001.2486039

Leili Afsah-Hejri, Elnaz Akbari, Arash Toudeshki, Taymaz Homayouni, Azar Alizadeh, and Reza Ehsani. 2020. Terahertz spectroscopy and imaging: A review on agricultural applications. *Comput. Electr. Agric.* 177 (2020), 105628. https://doi.org/10.1016/j.compag.2020.105628

Erkki Alarousu, Leszek Krehut, Tuukka Prykäri, and Risto Myllylä. 2005. Study on the use of optical coherence tomography in measurements of paper properties. *Measure. Sci. Technol.* 16, 5 (2005), 1131. https://doi.org/10.1088/0957-0233/16/5/012

T. Arecchi, M. Bellini, C. Corsi, R. Fontana, M. Materazzi, L. Pezzati, and A. Tortora. 2006. A new tool for painting diagnostics: Optical coherence tomography. *Optics Spectrosc.* 101, 1 (2006), 23–26. https://doi.org/10.1134/S0030400X06070058

Hidenobu Arimoto, Mariko Egawa, and Yukio Yamada. 2005. Depth profile of diffuse reflectance near-infrared spectroscopy for measurement of water content in skin. *Skin Res. Technol.* 11, 1 (2005), 27–35. https://doi.org/10.1111/j.1600-0846.2005.00093.x

Caroline R. Baumal. 1999. Clinical applications of optical coherence tomography. *Curr. Opin. Ophthalmol.* 10, 3 (1999), 182–188.

Amos Beimel. 2011. Secret-sharing schemes: A survey. In *Proceedings of the International Conference on Coding and Cryptology*. Springer, 11–46. https://doi.org/10.1007

David A. Boas, Dana H. Brooks, Eric L. Miller, Charles A. DiMarzio, Misha Kilmer, Richard J. Gaudette, and Quan Zhang. 2001. Imaging the body with diffuse optical tomography. *IEEE Signal Process. Mag.* 18, 6 (2001), 57–75. https://doi.org/10.1109/79.962278

Alan C. Bovik. 2009. Basic binary image processing. In *The Essential Guide to Image Processing*. Elsevier, 69–96. https://doi.org/10.1016/B978-0-12-374457-9.00004-4

Ginger Butcher. 2010. *Tour of the Electromagnetic Spectrum*. National Aeronautics and Space Administration.

Perumal Varun Chadalavada, Goutham Palaniappan, Vimal Kumar Chandran, Khai Truong, and Daniel Wigdor. 2018. ID'em: Inductive sensing for embedding and extracting information in robust materials. *Proc. ACM Interact. Mobile Wear. Ubiq. Technol.* 2, 3 (2018), 1–28. https://doi.org/10.1145/3264907

Vincent Chan and Anahi Perlas. 2011. Basics of ultrasound imaging. In *Atlas of Ultrasound-guided Procedures in Interventional Pain Management*. Springer, 13–19. https://doi.org/10.1007/978-1-4419-1681-5_2

Jakub Czajkowski, Tuukka Prykäri, Erkki Alarousu, Jaakko Palosaari, and Risto Myllylä. 2010. Optical coherence tomography as a method of quality inspection for printed electronics products. *Optic. Rev.* 17, 3 (2010), 257–262. https://doi.org/10.1007/s10043-010-0045-0

Jana Dambrogio, Amanda Ghassaei, Daniel Starza Smith, Holly Jackson, Martin L. Demaine, Graham Davis, David Mills, Rebekah Ahrendt, Nadine Akkerman, David van der Linden, et al. 2021. Unlocking history through automated virtual unfolding of sealed documents imaged by X-ray microtomography. *Nature Commun.* 12, 1 (2021), 1–10. https://doi.org/10.1038/s41467-021-21326-w

Niranjan Damera-Venkata and Nelson L. Chang. 2009. Display supersampling. *ACM Trans. Graph.* 28, 1 (2009), 1–19. https://doi.org/10.1145/1477926.1477935

Yiming Deng and Xin Liu. 2011. Electromagnetic imaging methods for nondestructive evaluation applications. *Sensors* 11, 12 (2011), 11774–11808.

Nicolas Ducros, Juan Felipe Perez-Juste Abascal, Bruno Sixou, Simon Rit, and Françoise Peyrin. 2017. Regularization of nonlinear decomposition of spectral x-ray projection images. *Med. Phys.* 44, 9 (2017), e174–e187.

Adolf F. Fercher, Wolfgang Drexler, Christoph K. Hitzenberger, and Theo Lasser. 2003. Optical coherence tomography-principles and applications. *Reports Progr. Phys.* 66, 2 (2003), 239.

S. Geetha, K. K. Satheesh Kumar, Chepuri R. K. Rao, M. Vijayan, and D. C. Trivedi. 2009. EMI shielding: Methods and materials-A review. *J. Appl. Polymer Sci.* 112, 4 (2009), 2073–2086. https://doi.org/10.1002/app.29812

S. Gholizadeh. 2016. A review of non-destructive testing methods of composite materials. *Procedia Struct. Integr.* 1 (2016), 50–57.

Mayank Goel, Eric Whitmire, Alex Mariakakis, T. Scott Saponas, Neel Joshi, Dan Morris, Brian Guenter, Marcel Gavriliu, Gaetano Borriello, and Shwetak N. Patel. 2015. HyperCam: Hyperspectral imaging for ubiquitous computing applications. In *Proceedings of the ACM International Joint Conference on Pervasive and Ubiquitous Computing (UbiComp'15)*. ACM, New York, NY, 145–156. https://doi.org/10.1145/2750858.2804282

Lewis D. Griffin, Matthew Caldwell, Jerone T. A. Andrews, and Helene Bohler. 2018. "unexpected item in the bagging area" Anomaly detection in x-ray security images. *IEEE Trans. Info. Forensics Secur.* 14, 6 (2018), 1539–1553.

E. J. Hall and D. J. Brenner. 2008. Cancer risks from diagnostic radiology. *Brit. J. Radiol.* 81, 965 (2008), 362–378. https://doi.org/10.1259/bjr/01948454

M. Hegedüs, K. Fedorov, I. Antonov, P. Karataev, and V. N. Antonov. 2020. Detection of black body radiation using a compact terahertz imager. *Appl. Phys. Lett.* 117, 23 (2020), 231106. https://doi.org/10.1063/5.0022533

Cristian Herrojo, Ferran Paredes, and Ferran Martín. 2019a. Double-stub loaded microstrip line reader for very high data density microwave encoders. *IEEE Trans. Microw. Theory Techn.* 67, 9 (2019), 3527–3536. https://doi.org/10.1109/TMTT.2019.2929128

Cristian Herrojo, Ferran Paredes, Javier Mata-Contreras, and Ferran Martín. 2019b. Chipless-RFID: A review and recent developments. *Sensors* 19, 15 (2019), 3385. https://doi.org/10.3390/s19153385

Yoko Hoshi and Yukio Yamada. 2016. Overview of diffuse optical tomography and its clinical applications. *J. Biomed. Optics* 21, 9 (2016), 091312.

David Huang, Eric A. Swanson, Charles P. Lin, Joel S. Schuman, William G. Stinson, Warren Chang, Michael R. Hee, Thomas Flotte, Kenton Gregory, Carmen A. Puliafito et al. 1991. Optical coherence tomography. *Science* 254, 5035 (1991), 1178–1181. https://doi.org/10.1126/science.1957169

Christian Jansen, Steffen Wietzke, Ole Peters, Maik Scheller, Nico Vieweg, Mohammed Salhi, Norman Krumbholz, Christian Jördens, Thomas Hochrein, and Martin Koch. 2010. Terahertz imaging: Applications and perspectives. *Appl. Optics* 49, 19 (2010), E48–E57.

Weiwei Jiang, Gabriele Marini, Niels van Berkel, Zhanna Sarsenbayeva, Zheyu Tan, Chu Luo, Xin He, Tilman Dingler, Jorge Goncalves, Yoshihiro Kawahara, and Vassilis Kostakos. 2019. Probing sucrose contents in everyday drinks using miniaturized near-infrared spectroscopy scanners. *Proc. ACM Interact. Mob. Wearable Ubiquitous Technol.* 3, 4, Article 136 (Dec. 2019), 25 pages. https://doi.org/10.1145/3369834

Weiwei Jiang, Zhanna Sarsenbayeva, Niels van Berkel, Chaofan Wang, Difeng Yu, Jing Wei, Jorge Goncalves, and Vassilis Kostakos. 2021. User trust in assisted decision-making using miniaturized near-infrared spectroscopy. In *Proceedings of the CHI Conference on Human Factors in Computing Systems*. Association for Computing Machinery, New York, NY, 1–16. https://doi.org/10.1145/3411764.3445710

Yoshihiro Kawahara, Steve Hodges, Benjamin S. Cook, Cheng Zhang, and Gregory D. Abowd. 2013. Instant inkjet circuits: Lab-based inkjet printing to support rapid prototyping of ubicomp devices. In *Proceedings of the ACM International Joint Conference on Pervasive and Ubiquitous Computing*. 363–372. https://doi.org/10.1145/2493432.2493486

Aditya Khosla, Nityananda Jayadevaprakash, Bangpeng Yao, and Li Fei-Fei. 2011. Novel dataset for fine-grained image categorization. In *Proceedings of the 1st Workshop on Fine-Grained Visual Categorization, IEEE Conference on Computer Vision and Pattern Recognition*.

Su-Hwan Kim, Jee-Hyun Kim, and Shin-Won Kang. 2011. Nondestructive defect inspection for LCDs using optical coherence tomography. *Displays* 32, 5 (2011), 325–329. https://doi.org/10.1016/j.displa.2011.04.002

Simon Klakegg, Jorge Goncalves, Chu Luo, Aku Visuri, Alexey Popov, Niels van Berkel, Zhanna Sarsenbayeva, Vassilis Kostakos, Simo Hosio, Scott Savage, et al. 2018. Assisted medication management in elderly care using miniaturised near-infrared spectroscopy. In *Proceedings of the ACM on Interactive, Mobile, Wearable and Ubiquitous Technologies*. 69. https://doi.org/10.1145/3214272

Simon Klakegg, Jorge Goncalves, Niels van Berkel, Chu Luo, Simo Hosio, and Vassilis Kostakos. 2017. Towards commoditised near infrared spectroscopy. In *Proceedings of the Conference on Designing Interactive Systems (DIS'17)*. ACM, New York, NY, 515–527. https://doi.org/10.1145/3064663.3064738

Simon Klakegg, Chu Luo, Jorge Goncalves, Simo Hosio, and Vassilis Kostakos. 2016. Instrumenting smartphones with portable NIRS. In *Proceedings of the ACM International Joint Conference on Pervasive and Ubiquitous Computing: Adjunct (UbiComp'16)*. ACM, New York, NY, 618–623. https://doi.org/10.1145/2968219.2971590

Marcin Kowalski, Mariusz Kastek, Michal Walczakowski, Norbert Palka, and Mieczyslaw Szustakowski. 2015. Passive imaging of concealed objects in terahertz and long-wavelength infrared. *Appl. Optics* 54, 13 (2015), 3826–3833. https://doi.org/10.1364/AO.54.003826

Dingzeyu Li, Avinash S. Nair, Shree K. Nayar, and Changxi Zheng. 2017. Aircode: Unobtrusive physical tags for digital fabrication. In *Proceedings of the 30th Annual ACM Symposium on User Interface Software and Technology*. 449–460. https://doi.org/10.1145/3126594.3126635

Ai Liu, Gang Li, Zhigang Fu, Yang Guan, and Ling Lin. 2018. Non-linearity correction in NIR absorption spectra by grouping modeling according to the content of analyte. *Sci. Rep.* 8, 1 (2018), 1–10. https://doi.org/10.1038/s41598-018-26802-w

Jonathan Long, Evan Shelhamer, and Trevor Darrell. 2015. Fully convolutional networks for semantic segmentation. In *Proceedings of the IEEE Conference on Computer Vision and Pattern Recognition (CVPR'15)*.

Ilya Loshchilov and Frank Hutter. 2017. Decoupled weight decay regularization. Retrieved from https://arXiv:1711.05101.

Yongsen Ma, Gang Zhou, and Shuangquan Wang. 2019. WiFi sensing with channel state information: A survey. *ACM Comput. Surveys* 52, 3 (2019), 1–36. https://doi.org/10.1145/3310194

Harry E. Martz, Clint M. Logan, Daniel J. Schneberk, and Peter J. Shull. 2016. *X-ray Imaging: Fundamentals, Industrial Techniques and Applications*. CRC Press.

Peter Meszaros. 2006. Gamma-ray bursts. *Rep. Progr. Phys.* 69, 8 (2006), 2259.

Peter G. Morris. 1986. Nuclear magnetic resonance imaging in medicine and biology. (1986).

E. W. T. Ngai, Karen K. L. Moon, Frederick J. Riggins, and Y. Yi Candace. 2008. RFID research: An academic literature review (1995–2005) and future research directions. *Int. J. Product. Econ.* 112, 2 (2008), 510–520. https://doi.org/10.1016/j.ijpe.2007.05.004

M.-E. Nilsback and A. Zisserman. 2006. A visual vocabulary for flower classification. In *Proceedings of the IEEE Computer Society Conference on Computer Vision and Pattern Recognition (CVPR'06)*, Vol. 2. 1447–1454. https://doi.org/10.1109/CVPR.2006.42

Vasilis Ntziachristos. 2010. Going deeper than microscopy: The optical imaging frontier in biology. *Nature Methods* 7, 8 (2010), 603–614. https://doi.org/10.1038/nmeth.1483

Sonia H. Contreras Ortiz, Tsuicheng Chiu, and Martin D. Fox. 2012. Ultrasound image enhancement: A review. *Biomed. Signal Process. Control* 7, 5 (2012), 419–428. https://doi.org/10.1016/j.bspc.2012.02.002

Vishal M. Patel, Joseph N. Mait, Dennis W. Prather, and Abigail S. Hedden. 2016. Computational millimeter wave imaging: Problems, progress, and prospects. *IEEE Signal Process. Mag.* 33, 5 (2016), 109–118. https://doi.org/10.1109/MSP.2016.2581206

Stevan Preradovic and Nemai Chandra Karmakar. 2010. Chipless RFID: Bar code of the future. *IEEE Microw. Mag.* 11, 7 (2010), 87–97. https://doi.org/10.1109/MMM.2010.938571

Albert Redo-Sanchez, Barmak Heshmat, Alireza Aghasi, Salman Naqvi, Mingjie Zhang, Justin Romberg, and Ramesh Raskar. 2016. Terahertz time-gated spectral imaging for content extraction through layered structures. *Nature Commun.* 7, 1 (2016), 1–7. https://doi.org/10.1038/ncomms12665

Gabriele Reich. 2005. Near-infrared spectroscopy and imaging: Basic principles and pharmaceutical applications. Non-Invasive Spectroscopic and Imaging Techniques in Drug Delivery. *Adv. Drug Deliv. Rev.* 57, 8 (2005), 1109–1143. https://doi.org/10.1016/j.addr.2005.01.020

Yves Roggo, Pascal Chalus, Lene Maurer, Carmen Lema-Martinez, Aurélie Edmond, and Nadine Jent. 2007. A review of near infrared spectroscopy and chemometrics in pharmaceutical technologies. *J. Pharm. Biomed. Anal.* 44, 3 (2007), 683–700.

Olaf Ronneberger, Philipp Fischer, and Thomas Brox. 2015. U-Net: Convolutional networks for biomedical image segmentation. In *Medical Image Computing and Computer-Assisted Intervention (MICCAI'15)*, Nassir Navab, Joachim Hornegger, William M. Wells, and Alejandro F. Frangi (Eds.). Springer International Publishing, Cham, 234–241.

Kurt Rossmann. 1969. Point spread-function, line spread-function, and modulation transfer function. *Radiology* 93, 2 (1969), 257–272. https://doi.org/10.1148/93.2.257 PMID: 5822701.

Z. Sabetsarvestani, Barak Sober, Catherine Higgitt, Ingrid Daubechies, and M. R. D. Rodrigues. 2019. Artificial intelligence for art investigation: Meeting the challenge of separating X-ray images of the Ghent Altarpiece. *Sci. Adv.* 5, 8 (2019), eaaw7416. https://doi.org/10.1126/sciadv.aaw7416

T. W. L. Scheeren, P. Schober, and L. A. Schwarte. 2012. Monitoring tissue oxygenation by near infrared spectroscopy (NIRS): Background and current applications. *J. Clin. Monitor. Comput.* 26, 4 (2012), 279–287.

Quan Z. Sheng, Xue Li, and Sherali Zeadally. 2008. Enabling next-generation RFID applications: Solutions and challenges. *Computer* 41, 9 (2008), 21–28. https://doi.org/10.1109/MC.2008.386

Lawrence A. Shepp and Joseph Bernard Kruskal. 1978. Computerized tomography: The new medical X-ray technology. *Amer. Math. Monthly* 85, 6 (1978), 420–439.

Heinz W. Siesler, Yukihiro Ozaki, Satoshi Kawata, and H. Michael Heise. 2008. *Near-infrared Spectroscopy: Principles, Instruments, Applications.* John Wiley & Sons.

Douglas A. Skoog, Donald M. West, F. James Holler, and Stanley Crouch. 2013. *Fundamentals of Analytical Chemistry.* Nelson Education.

Erin Treacy Solovey, Audrey Girouard, Krysta Chauncey, Leanne M. Hirshfield, Angelo Sassaroli, Feng Zheng, Sergio Fantini, and Robert J. K. Jacob. 2009. Using fNIRS brain sensing in realistic HCI settings: Experiments and guidelines. In *Proceedings of the 22nd Annual ACM Symposium on User Interface Software and Technology.* ACM, 157–166.

Joo-Hiuk Son, Seung Jae Oh, and Hwayeong Cheon. 2019. Potential clinical applications of terahertz radiation. *J. Appl. Phys.* 125, 19 (2019), 190901. https://doi.org/10.1063/1.5080205

David Stifter. 2007. Beyond biomedicine: A review of alternative applications and developments for optical coherence tomography. *Appl. Phys. B* 88, 3 (2007), 337–357. https://doi.org/10.1007/s00340-007-2743-2

D. Stromer, V. Christlein, T. Schön, W. Holub, and A. Maier. 2017. Browsing through closed books: Evaluation of preprocessing methods for page extraction of a 3D CT book volume. In *Proceedings of the IOP Conference Series: Materials Science and Engineering*, Vol. 229. IOP Publishing, 012005. https://doi.org/10.1088/1757-899x/229/1/012005

Piotr Targowski, Bogumiła Rouba, Maciej Wojtkowski, and Andrzej Kowalczyk. 2004. The application of optical coherence tomography to non-destructive examination of museum objects. *Studies Conserv.* 49, 2 (2004), 107–114. https://doi.org/10.1179/sic.2004.49.2.107

George J. Tserevelakis, Margarita Tsagkaraki, Panagiotis Siozos, and Giannis Zacharakis. 2019. Uncovering the hidden content of layered documents by means of photoacoustic imaging. *Strain* 55, 2 (2019), e12289. https://doi.org/10.1111/str.12289

Andrew M. Wallace, Abderrahim Halimi, and Gerald S. Buller. 2020. Full waveform lidar for adverse weather conditions. *IEEE Trans. Vehic. Technol.* 69, 7 (2020), 7064–7077.

Xintao Wang, Ke Yu, Shixiang Wu, Jinjin Gu, Yihao Liu, Chao Dong, Yu Qiao, and Chen Change Loy. 2018. ESRGAN: Enhanced super-resolution generative adversarial networks. In *Proceedings of the European Conference on Computer Vision (ECCV'18).*

Zhou Wang and Alan C. Bovik. 2009. Mean squared error: Love it or leave it? A new look at signal fidelity measures. *IEEE Signal Process. Mag.* 26, 1 (2009), 98–117. https://doi.org/10.1109/MSP.2008.930649

Karl D. D. Willis and Andrew D. Wilson. 2013. InfraStructs: Fabricating information inside physical objects for imaging in the terahertz region. *ACM Trans. Graph.* 32, 4 (2013), 1–10. https://doi.org/10.1145/2461912.2461936

Cort J. Willmott and Kenji Matsuura. 2005. Advantages of the mean absolute error (MAE) over the root mean square error (RMSE) in assessing average model performance. *Climate Res.* 30, 1 (2005), 79–82. https://doi.org/10.3354/cr030079

Honami Yamane, Kazuo Tanaka, and Yoshiki Chujo. 2018. Synthesis of a near-infrared light-absorbing polymer based on thiophene-substituted Aza-BODIPY. *Polymer J.* 50, 3 (2018), 271–275. https://doi.org/10.1038/s41428-017-0014-6

Li Yang, Amin Rida, Rushi Vyas, and Manos M. Tentzeris. 2007. RFID tag and RF structures on a paper substrate using inkjet-printing technology. *IEEE Trans. Microw. Theory Techn.* 55, 12 (2007), 2894–2901. https://doi.org/10.1109/TMTT.2007.909886

Ali Zamanian and C. J. H. F. E. Hardiman. 2005. Electromagnetic radiation and human health: A review of sources and effects. *High Freq. Electr.* 4, 3 (2005), 16–26.

Yanzi Zhu, Yuanshun Yao, Ben Y. Zhao, and Haitao Zheng. 2017. Object recognition and navigation using a single networking device. In *Proceedings of the 15th Annual International Conference on Mobile Systems, Applications, and Services.* 265–277. https://doi.org/10.1145/3310194

Boris Zimmermann and Achim Kohler. 2013. Optimizing Savitzky-Golay parameters for improving spectral resolution and quantification in infrared spectroscopy. *Appl. Spectrosc.* 67, 8 (2013), 892–902.

Zhengxia Zou, Sen Lei, Tianyang Shi, Zhenwei Shi, and Jieping Ye. 2020. Deep adversarial decomposition: A unified framework for separating superimposed images. In *Proceedings of the IEEE/CVF Conference on Computer Vision and Pattern Recognition (CVPR'20).* 12803–12813. https://doi.org/10.1109/CVPR42600.2020.01282